Analysis Note
of the STAR Experiment

Measurement of particle production with Roman Pot detectors in diffractive proton-proton interactions at $\sqrt{s} = 200$ GeV

Leszek Adamczyk[1], Łukasz Fulek[1], Włodek Guryn[2], Bogdan Pawlik[3], Mariusz Przybycień[1], and Rafał Sikora[1]

[1]*AGH University of Science and Technology, FPACS, Kraków, Poland*
[2]*Brookhaven National Laboratory, Upton, NY, USA*
[3]*Institute of Nuclear Physics PAN, Kraków, Poland*

November 7, 2018

Abstract

In this note we present the analysis of the diffractive measurement with the STAR Roman Pot detectors at RHIC. The measurement is focused on the spectra of identified charged particles as pions, kaons, protons and their antiparticle counterparts in Single Diffraction Dissociation ($p + p \rightarrow p + X$) and Central Diffraction ($p + p \rightarrow p + X + p$) processes. The spectra of inclusive charged particles are also measured. Moreover, the proton–antiproton production asymmetry as a function of rapidity is presented and allows one to study the baryon number transfer over a large space in rapidity in single diffraction. A similar effect has been studied in proton-proton and proton-photon interactions but it is the first measurement in proton-Pomeron interaction. This data come from proton-proton collisions collected in 2015. The forward proton(s) were tagged in the STAR Roman Pot system while the charged particle tracks were reconstructed in the STAR Time Projection Chamber (TPC). Ionization energy loss of charged particles was used for particle identification. We describe all stages of the analysis involving the extraction of efficiency and acceptance corrections, comparison of the data with MC simulations and systematic uncertainty studies.

DRAFT

Contents

1. Introduction

1.1 Diffractive interactions in pp collisions

Diffractive processes at high energies are characterized by the exchange of the Pomeron, a color singlet object with quantum numbers of the vacuum described by the Regge theory [1][2]. Due to non-perturbative nature of interactions, there are difficulties in applying QCD to diffraction. Experimentally, diffraction is identified as interaction with large rapidity gap, i.e. final states are separated in rapidity space.

There are two processes of interest, shown in Figure 1.1 (a, b), the Central (CD: $p + p \to p + X + p$) and Single (SD: $p + p \to p + X$) Diffractive scattering, where X is the diffractive system. In CD interactions, two protons stay intact after the scattering, whereas in SD only one proton. The (identified) charged particle
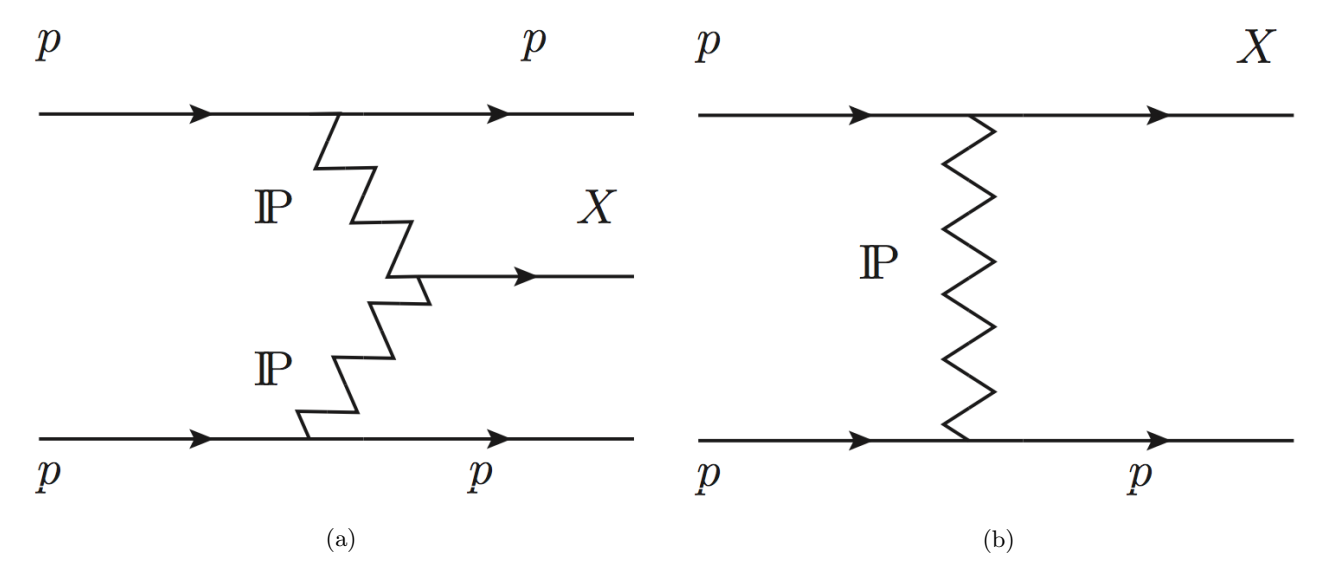

Figure 1.1: Diagrams of Central Diffraction (a) and Single Diffraction (b).

production in the mid-rapidity region has been widely studied in minimum bias inelastic hadron-hadron collisions starting from the very first experiments performed at ISR at CERN throughout contemporary measurements with very high center-of-mass energy at RHIC [3] and LHC [4]. This is the first measurement with tagged forward protons, which allows efficient identification of diffractive events. The measured particle spectra and ratios deliver information on collision dynamics, mechanism and allows to validate some phenomenological models and tune some general purpose MC generators.

1.2 Baryon number transfer

In the Standard Model the baryon number is conserved in all interactions. The conserved baryon number associated with the beam particles is called "baryon number transfer" and has been studied theoretically for some time [5, 6, 7]. The baryon number transfer, which is quantified by the baryon to anti-baryon ratios, is often described as a function of the size of the transport in rapidity represented by rapidy difference $\Delta y = y_{beam} - y$, where $y_{beam} = \ln\left(\sqrt{s}/m_p\right)$ is the rapidity of the beam and y the rapidity of the particles produced in the central system. In the String Junction Model [6] the baryon number can be transferred over large distances in the rapidity. In this picture, baryon number transfer is exponentially suppressed as a function of the rapidity interval Δy. In particular, when there are only purely gluonic exchanges between the valence quarks of the proton, the baryon number transfer does not depend on the rapidity and approaches a constant and finite value [5]. There is also a model [7], in which the initial baryon may end up at the backward end of the diffractive system. The edge of the rapidity gap $\Delta\eta$ is related to the relative proton momentum loss $\xi = \Delta E/E$, $\Delta\eta \approx -\ln\xi = -\ln\left(M_X^2/s\right)$. There is a large number of the experimental data available on baryon number

transfer [8]. The mid-rapidity anti-proton to proton ratio is sensitive to center-of-mass energy and varies between 0.4 for ISR energies and almost 1 for the LHC, where the transfer size in the rapidity space Δy is large and equals to almost 9 units. In addition, this effect was also measured by the H1 Collaboration in proton-photon interactions [9], where the data show that there is a sizeable baryon to anti-baryon asymmetry. The similar effect can be studied in SD interactions, where the direction of the initial baryon is uniquely defined.

2. Data set

2.1 Trigger

The main triggers designed for diffractive studies in Run 15 and used for the analysis described in this note are:

a) **SDT** for SD formed by the following conditions combined with the logical AND:

    1. RP_EOR || RP_WOR - signal in at least one RP on one side of the STAR central detector.

    2. Veto on any signal in small BBC tiles or ZDC on the outgoing proton side of the STAR central detector.

    3. At least two TOF hits.

b) **CPT2** for CD:

    1. (ET && !IT) || (!ET && IT) - signal in at least one RP on each side of the STAR central detector. A veto was introduced on signal in RPs above and below beamline.

    2. Veto on any signal in small BBC tiles or ZDC on any side of the STAR central detector.

    3. At least two TOF hits.

Above requirements were imposed in accordance with the diffractive events topology. Veto on any signal in small BBC tiles and ZDC allows to accept only events with rapidity gap and reject diffractive events with parallel pile-up event. The requirement of at least two TOF hits was to ensure activity in the mid-rapidity.

During Run 15 about 560 M CPT2 and 34 M SDT triggers were collected, which corresponds to 16.5 pb^{-1} and 16.9 nb^{-1} of integrated luminosity, repsectively. More information about number of events per run, prescales, rates, etc. can be found in the Ref. [10, 11].

2.2 Reconstruction

Raw data was processed with the library version SL17f with the following BFC options:

```
DbV20160418,pp2015c,btof,mtd,mtdCalib,pp2pp,-beamline,beamline3D,UseBTOFmatchOnly,VFStoreX,
fmsDat,fmsPoint,fpsDat,BEmcChkStat,-evout,CorrX,OSpaceZ2,OGridLeak3D,-hitfilt
```

The `UseBTOFmatchOnly` option was used to form the vertices only from the global TPC tracks matched with TOF hits. It was found that this option provides better signal reconstruction efficiency and resolutions. The study was performed with the same dataset processed with the SL15k library version and the details about it can be found in the Ref. [12].

The produced MuDst files (standard STAR data format) were further reduced to Cracow's picoDst data format. The details about picoDst format used in this analysis can be found in the Ref. [13].

3. Analysis

3.1 Event selection

3.1.1 SD and CD

1. Exactly one primary vertex with TPC tracks matched with hits in TOF.

2. The reconstructed vertex is required to be within 80 cm of the detector center along the beam direction.

3. At least two primary TPC tracks $N_{reco}^{primary}$ matched with hits in TOF and satisfying the selection criteria described in 3.2.

4. If there are exactly two primary tracks satisfying the above criteria and exactly two global tracks used for vertexing (Table 3.2), the longitudinal distance between these tracks $|\Delta z_0| < 2$ cm.

3.1.2 SD

1. SDT trigger

2. RP trigger on only one side of the STAR central detector (veto EAST && WEST)

3. RP trigger on only UP or DOWN stations (veto UP && DOWN)

4. Any signal in small BBC tiles or ZDC on the opposite side of the STAR central detector to the triggered RP station(s).

5. RP trigger on exactly two RP stations.

6. Exactly one RP global track in the above RP stations with proton fractional momentum loss $0.02 < \xi < 0.4$.

3.1.3 CD

1. CPT2 trigger

2. Exactly one RP global track on each side of the STAR central detector with proton fractional momentum loss $0.02 < \xi_1, \xi_2 < 0.4$.

3.2 Track selection

For this analysis several track quality cuts are applied as shown in Table 3.1. Tracks are required to have at least 25 fit points, ratio of fit points to possible fit points $N_{fit}/N_{poss} > 0.52$, 15 dE/dx points, transverse impact parameter $d_0 < 1.5$ cm, and have a $\text{DCA}_{xy} < 1.5$ cm, $\text{DCA}_z < 1$ cm. Tracks are accepted within a pseudorapidity window of -0.7 to 0.7. The cuts listed in the Table 3.1 on the number of Fit Points and ratio of Fit Points over Possible Fit Points are standard cuts used to reject low quality TPC tracks and avoid track splitting effects. The global DCA cut is used to select tracks that originate from the primary interaction vertex. The cut on dE/dx points is used to ensure that selected tracks have sufficient energy loss information for particle identification purposes. Singly charged particles must have a minimum p_T of 0.15 GeV/c to exit the TPC in the 0.5 Tesla magnetic field. In this analysis tracks are required to have $p_T > 0.2$ GeV/c. For the identified particle results in this paper, the pseudorapidity region is restricted within $|\eta| < 0.7$ (i.e. mid-rapidity). The full 2π azimuthal coverage of the TPC is utilized.

| Quantity	Cut
Number of Fit Points	Fit Points > 24
Transverse Impact Parameter	$|d_0| < 1.5$ cm
Global Track Distance of Closest Approach to the primary vertex	$DCA_{xy} < 1.5$ cm, $|DCA_z| < 1.$ cm
Ratio of Fit Points / Possible Fit Points	Fit Points/ Possible Fit Points > 0.52
dE/dx Fit Points	dE/dx Fit Points > 14
Primary Track Transverse Momentum	$p_T > 0.2$ GeV/c
Pseudorapidity	$|\eta| < 0.7$
TOF Matched Track	TOF Match-Flag ≥ 1

Table 3.1: Analysis Track Level Cuts
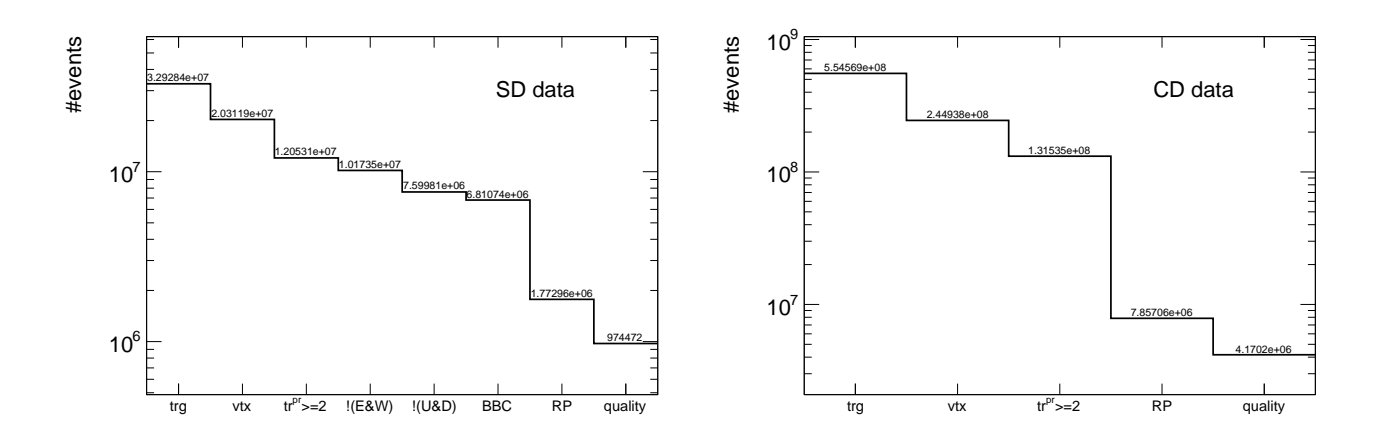
Figure 3.1: Number of accepted events after applying each event selection cut.

3.3 Accidental background study

The accidental backgrounds (same bunch pile-up background) are quantified using data-driven method. This includes any single(double)-side proton signal collected in coincidence with a diffractive like signal in the TPC-TOF detector. This type of background may come from the overlap of:

1. RP:

   - proton from beamhalo,
   - low mass SD process without activity in TOF,
   - elastic or low mass CD processes with undetected proton on the other side,

2. TPC+TOF:

   - any central activity (dominantly from ND events).

3.3.1 Proton overlay probability

The probability of observing the protons passing the RP proton track selection of the analysis was calculated from **Zerobias** trigger sample. As being assumed to be uncorrelated to the TPC-TOF activity, the probability is used to quantify the addition of an extra-proton to any kind of events. Figure 3.2a shows the derived probabilities of getting global and local proton tracks in SD. The probabilities of observing two protons on the opposite sides of the IP in CD using only proton global tracks were shown in the Figure 3.2b. The main contribution to the accidental background in CD comes from the elastic RP configuration, where it is dominated by elastic (halo), elastic and SD, halo and SD protons and its probability equals to about 0.2%.
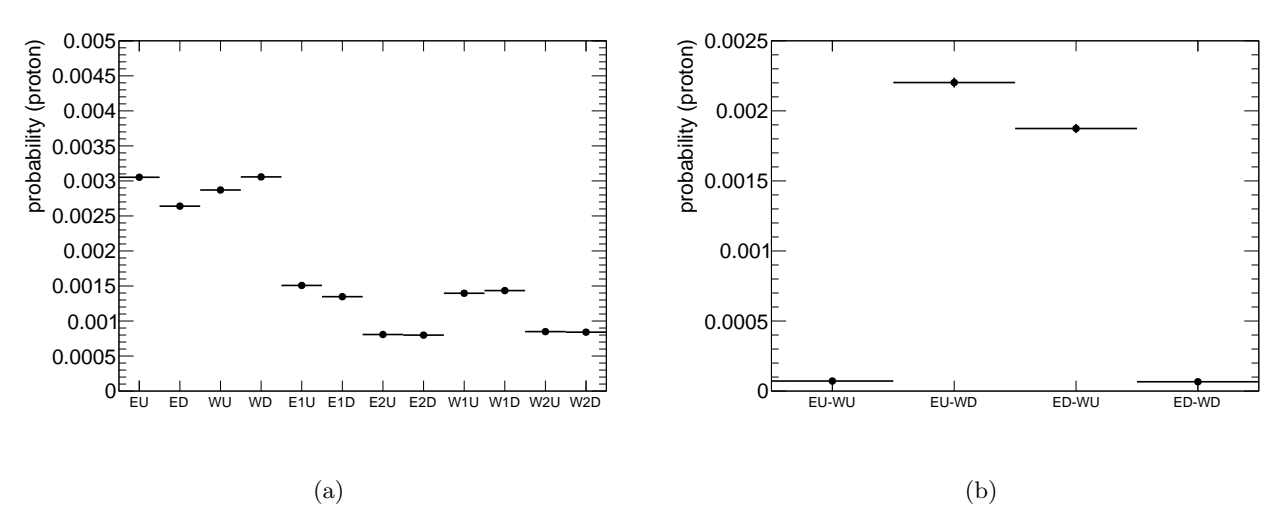
(a)	(b)

Figure 3.2: Proton overlay probability calculated from **Zerobias** trigger sample for SD (a) and CD (b, only proton global tracks used). The probability to observe accidental global tracks in RP in SD varies between $0.25 - 0.3\%$. Most of the accidental background in CD comes from the elastic RP configuration.

3.3.2 Accidental background in SD

The background from accidentals in SD events was calculated from the **Zerobias** sample multiplied by the probability of observing the accidental proton track in the RP and corrected by the relevant trigger prescales $\frac{PS^{Zerobias}}{PS^{SDT}}$. Figure 3.3 shows the proton hit position in E1U with the data-driven background contribution for the region of interest (a,b - proton global and local tracks; c,d - only proton global tracks).
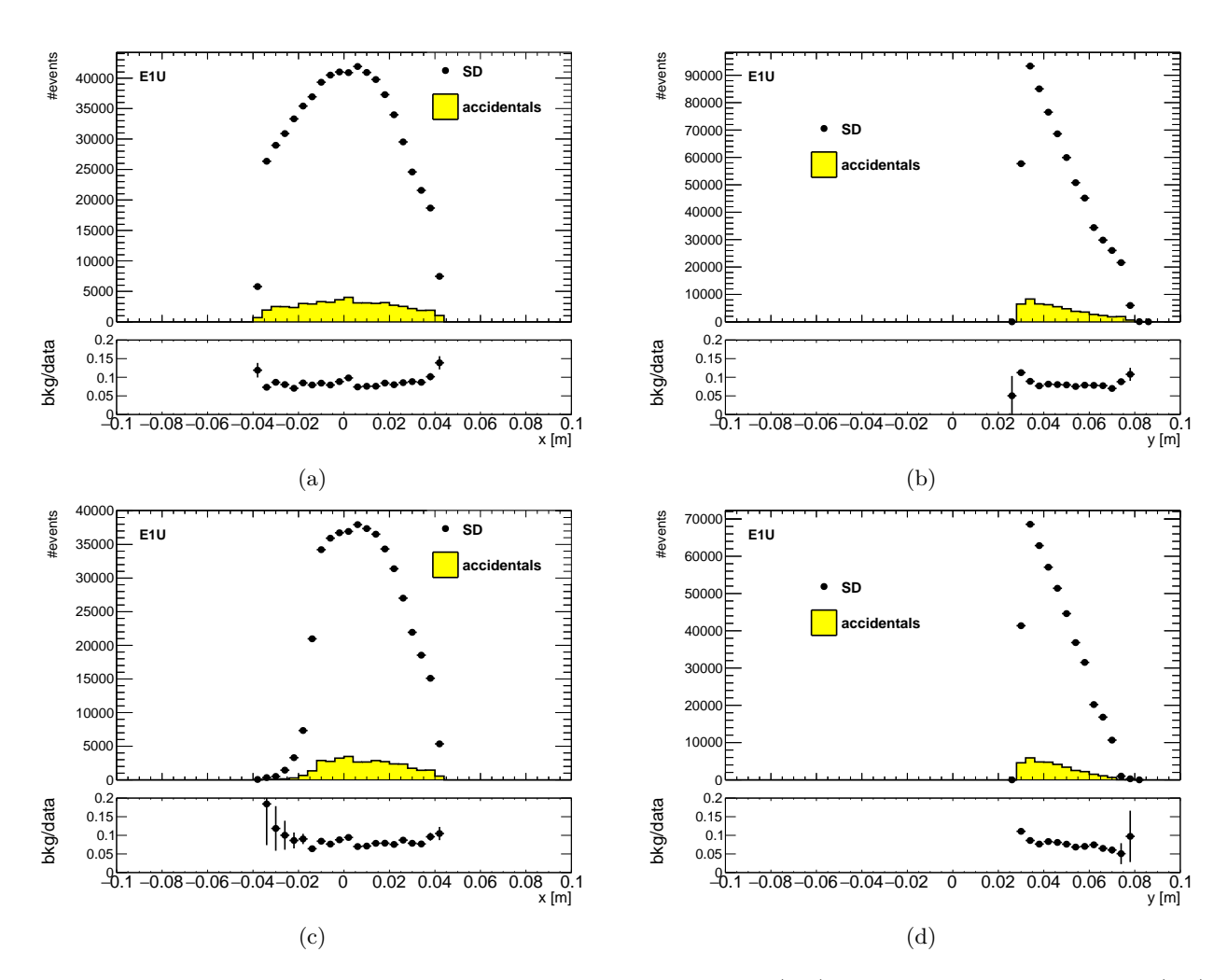
Figure 3.3: Proton hit position in SD using global+local proton tracks (a-b) and only global proton tracks (c-d). The background contribution equals to about 10%.

Due to observe the same accidental backround contribution for global and global+local proton track ($\approx 10\%$), also the $-t$ and ξ distributions were checked (Figure 3.4). To reconstruct properly $-t$ and ξ only global proton tracks were used. The flat background was observed in the $-t$ distribution. However, the ξ distribution shows that most of the background is located around $\xi \approx 0$, which confirms the assumption that most of the accidental background comes from elastic, beam halo or low mass diffractive protons.
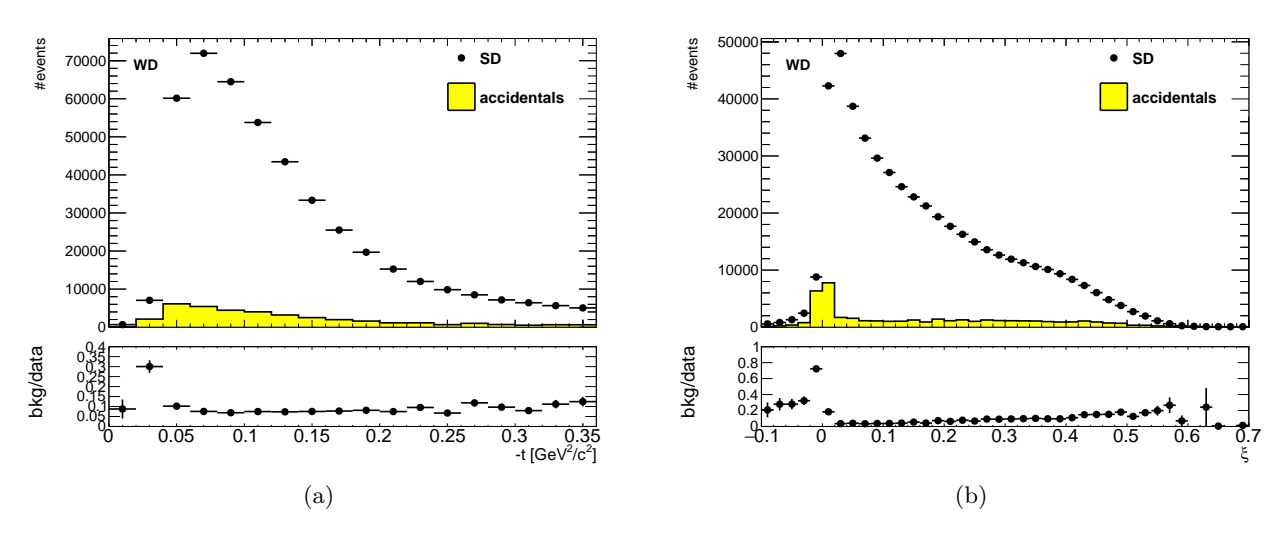

Figure 3.4: $-t$ and ξ distribution for WD arm in SD. Accidental background suppressed for $0.02 < \xi < 0.4$.

Additionally, the background begins to rise at $\xi \approx 0.4$. This probably comes from true or fake tracks

reconstructed in RP arising from showers happening outside the RP stations. Finally, the additional proton selection cuts were obtained for SD - the proton track is required to be a global track with $0.02 < \xi < 0.4$. The probability to observe the accidental proton in RP decreased to about 0.15% (Figure 3.5a) and the accidental background contribution is about $5 - 10\%$ (Figure 3.5b).

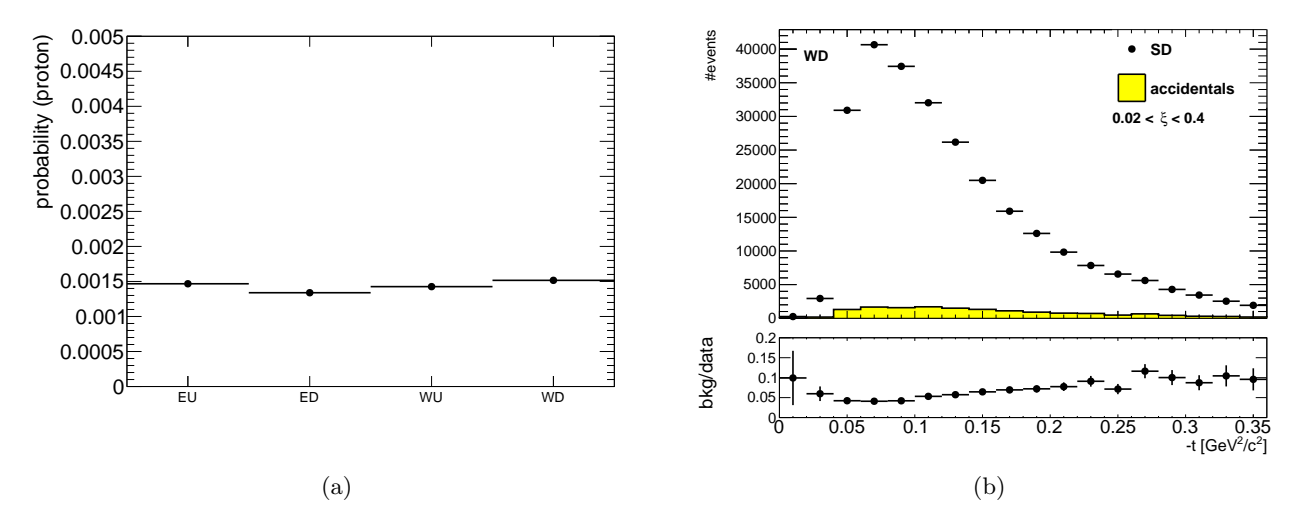(a)   (b)

Figure 3.5: Proton overlay probability (a) and $-t$ (b) distribution for SD events with $0.02 < \xi < 0.4$. The probability to observe accidental proton in RP decreased to about 0.15%.
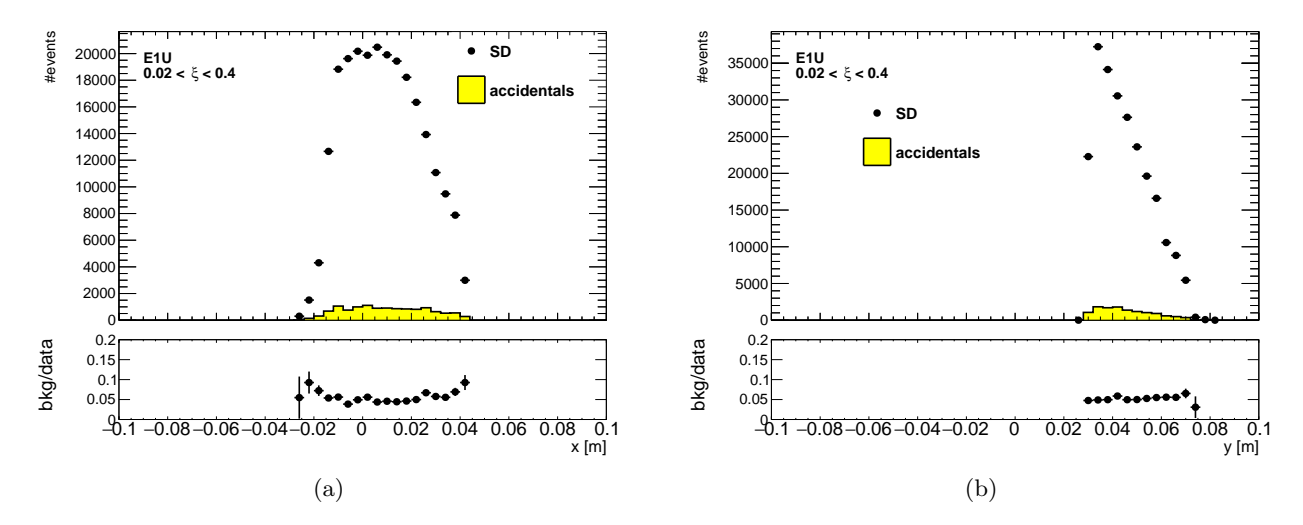

(a)   (b)

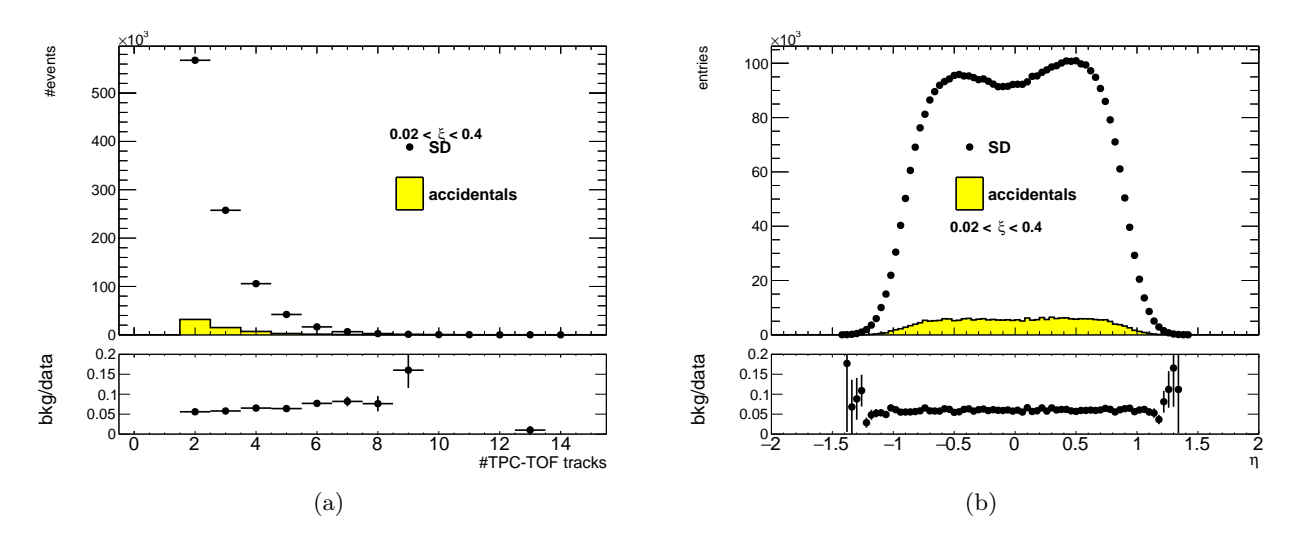Figure 3.6: Proton hit position in E1U for SD events with $0.02 < \xi < 0.4$.

(a)

(b)

Figure 3.7: TPC-TOF related variables (TPC-TOF track multiplicity and η of those tracks) for SD events with $0.02 < \xi < 0.4$. The background contribution is about $5 - 10\%$.

3.3.3 Accidental background in CD

The background from accidentals in CD events was calculated in the similar way to the SD. Only proton global tracks were used to calculate the probability of observing two accidental protons on the opposite sides of the IP. Figure 3.8 shows the collinearity distributions for inelastic (a) and elastic (b) RP configuration.
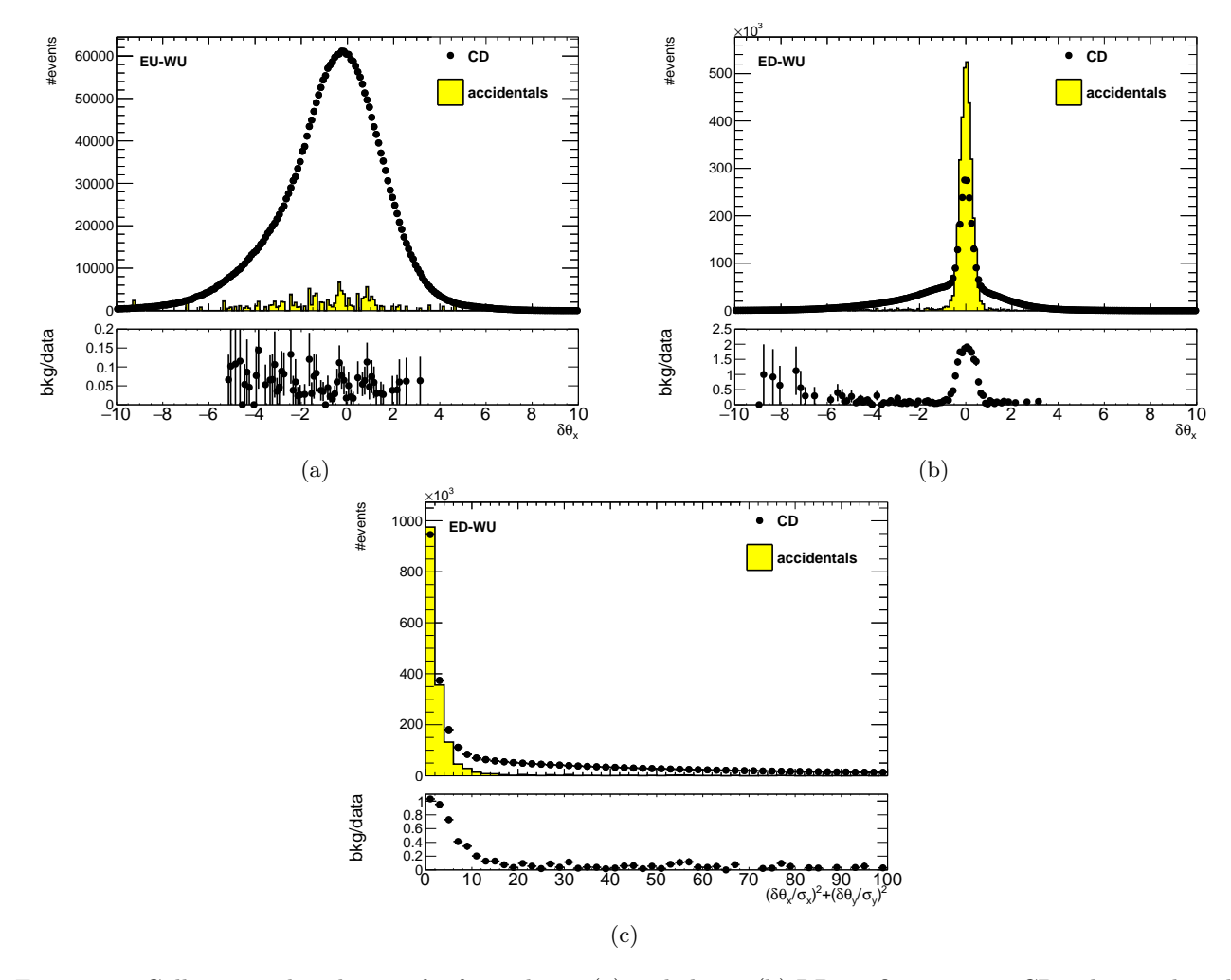

(a)

(b)

(c)

Figure 3.8: Collinearity distribution θ_X for inelastic (a) and elastic (b) RP configuration in CD. The accidental background for elastic configuration is overestimated. The background was normalized to the signal in the first bin of the collinearity distribution (c).

12

The accidental background for the elastic configuration excess the 100% and is overestimated. Two solutions were found to estimate the background in the elastic RP configuration:

1. Require the protons to be anti-collinear $\left((\delta\theta_x/\sigma_x)^2 + (\delta\theta_y/\sigma_y)^2 > 3^2\right)$.
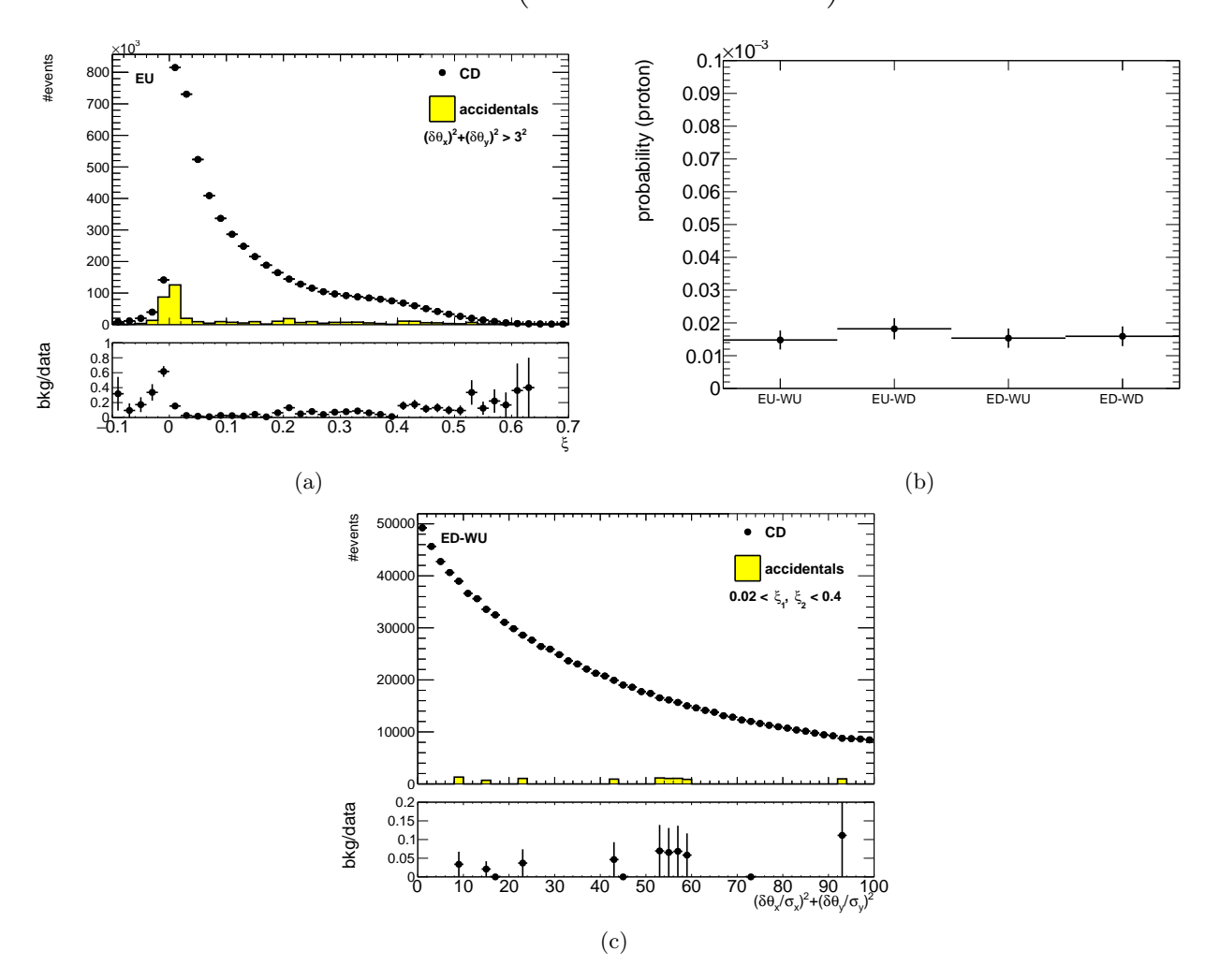

(a)

(b)

(c)

Figure 3.9: ξ distribution of protons in EU arm with anti-collinearity cut. The background is suppressed for $0.02 < \xi_1, \xi_2 < 0.4$ and the proton overlay probability is reduced to $2 \cdot 10^{-5}$. The accidental background contribution was reduced to about 5% with this cut.

The ξ distribution with anti-collinearity cut, as shown in Figure 3.9a, was checked and it was found that the proton tracks should be required to be global tracks with $0.02 < \xi_1, \xi_2 < 0.4$. With this cuts the probability of observing two accidental protons was reduced to about $2 \cdot 10^{-5}$ for all RP configurations (Figure 3.9b). Additionally, the overestimation of the background was not observed in the collinearity distribution (Figure 3.9c) and the accidental background contribution decreased to about 5%.
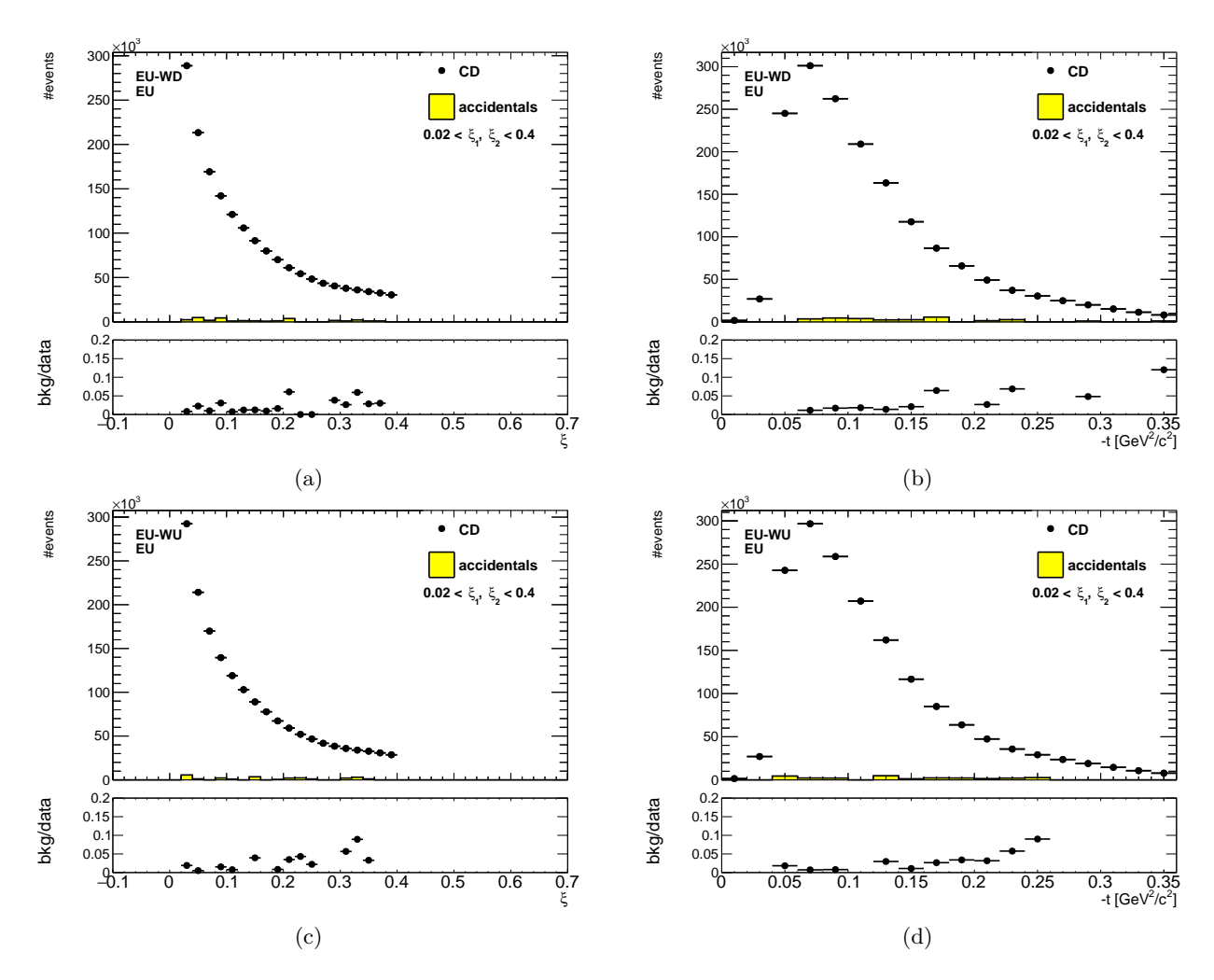
Figure 3.10: ξ and $-t$ in elastic and inelastic RP configuration measured with EU. The background is reduced to about 5% in both RP configurations.

2. Normalize the background to the signal in the first bin of the collinearity distribution (Figure 3.8c). Here it was assumed that all collinear protons are background protons and the upper limit for the background was set. Also the scale factor for the background was found. Similar to the first method, it was found that the background is supressed for $0.02 < \xi_1, \xi_2 < 0.4$ and varies between $2-3\%$ (Figure 3.11 b-d). The collinearity cut is not required anymore.
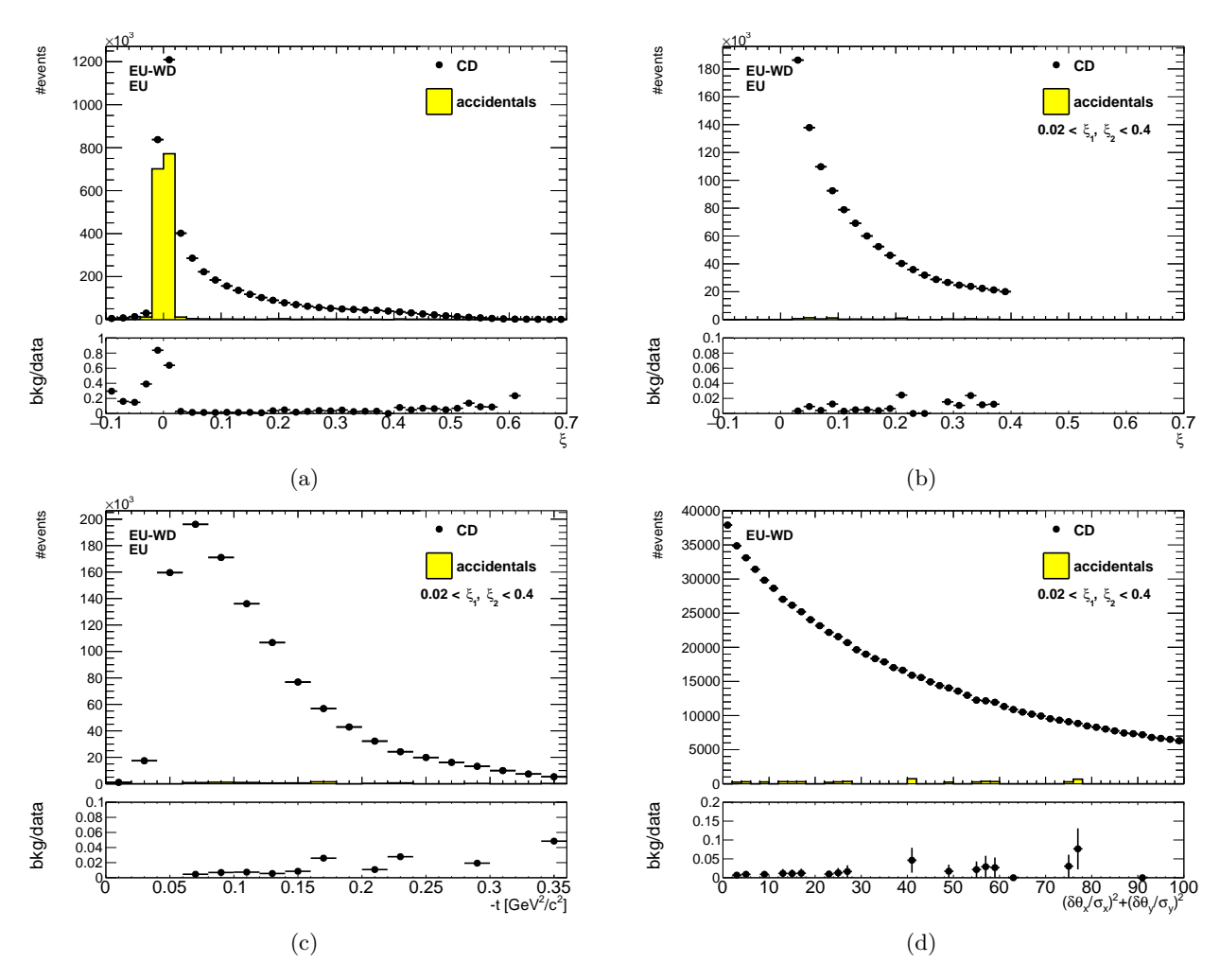
(a)

(b)

(c)

(d)

Figure 3.11: ξ distribution in CD with the accidental background normalized to the signal in the first bin of the collinearity distribution (Figure 3.8c). Most of the accidental background located outside the $0.02 < \xi_1, \xi_2 < 0.4$ region. The background reduced to about $2-3\%$ in ξ, $-t$ and collinearity distributions with $0.02 < \xi_1, \xi_2 < 0.4$ cut applied.
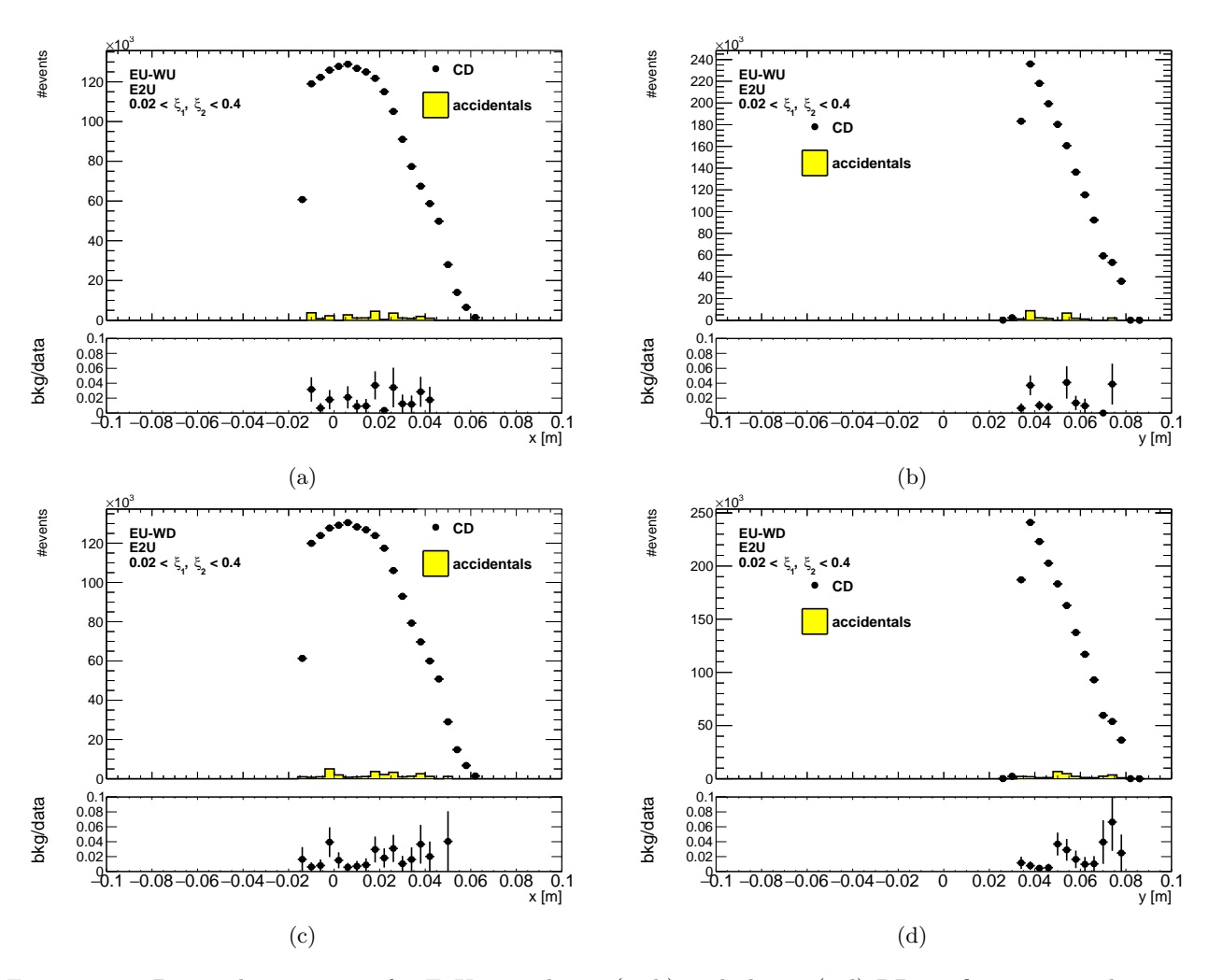
(a)

(b)

(c)

(d)

Figure 3.12: Proton hit positions for E2U in inelastic (a, b) and elastic (c,d) RP configuration with $0.02 < \xi_1, \xi_2 < 0.4$ cut applied. The background reduced to about $2 - 4\%$ in both RP configurations.
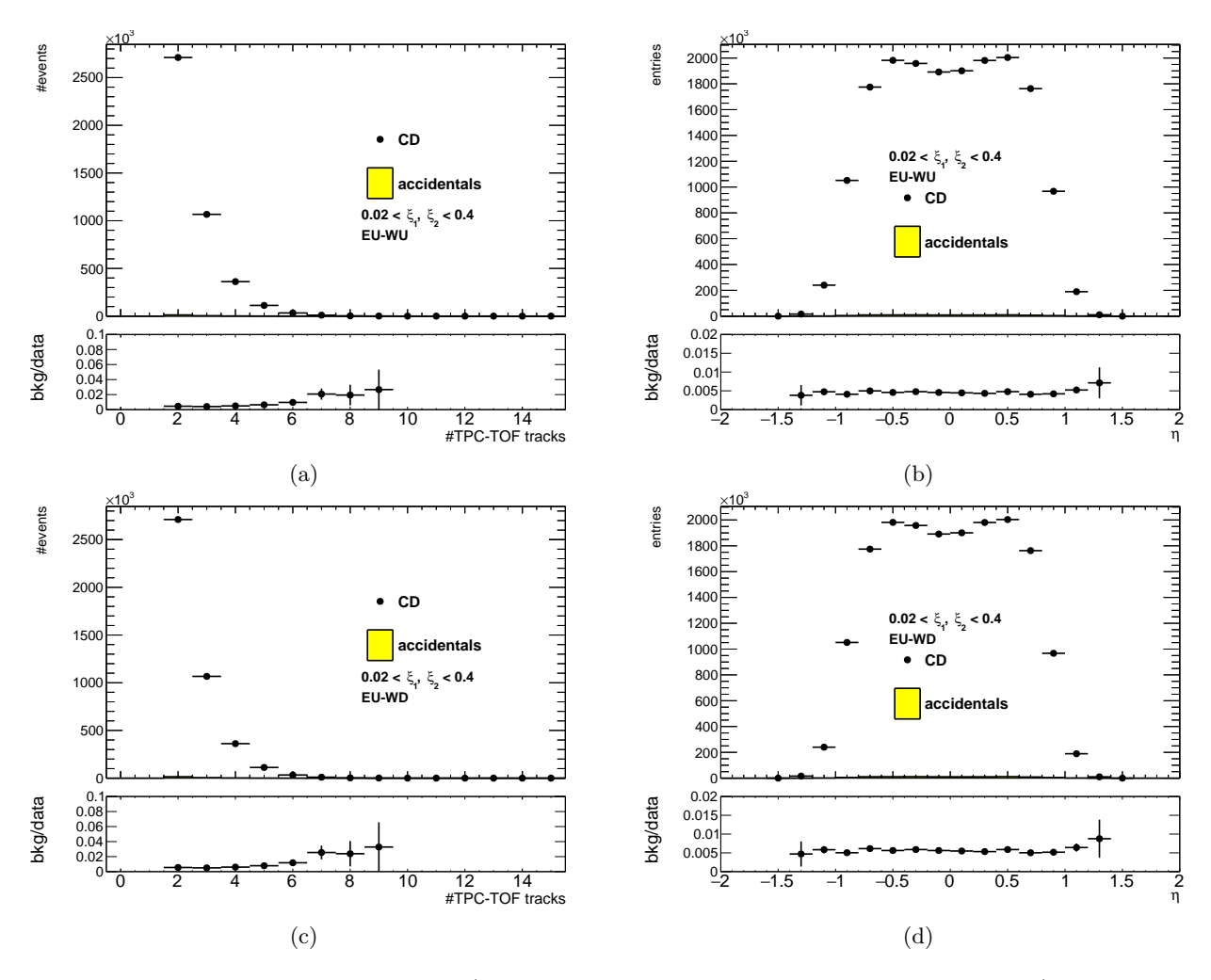
(a)

(b)

(c)

(d)

Figure 3.13: TPC-TOF related variables (TPC-TOF track multiplicity and η of those tracks) for CD events with $0.02 < \xi_1, \xi_2 < 0.4$. The background contribution is about 0.5%.

3.3.4   TPC related distributions with additional proton selection cuts

The additional proton selection $\xi\,(\xi_1, \xi_2)$ cuts reduce the statistics of about 20% and 50% for SD and CD, respectively. The most significant background reduction was observed mainly in CD. Figure 3.14 shows the comparison of the p_T (c, f) and η (b, e) distibutions with and without the $\xi\,(\xi_1, \xi_2)$ cuts applied. In spite of the reduction of the background, the shape of those distributions did not change. Although, the TPC-TOF track multiplicity distribution changed with above cuts applied (Figure 3.14 a, d). The rest of the accidental background has to be subtracted statistically.
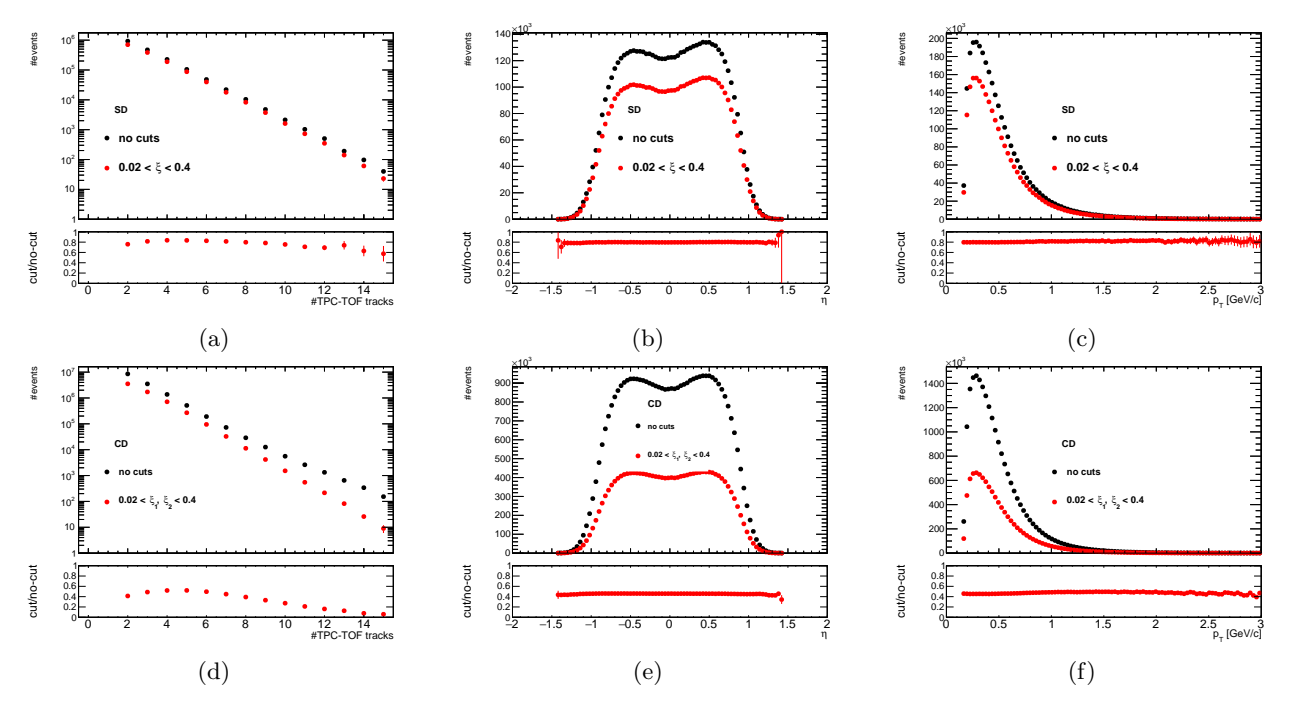
Figure 3.14: TPC-TOF related distributions with and without additional proton track selection cuts applied in SD (a-c) and CD (d-f). The additional proton selection ξ (ξ_1, ξ_2) cuts reduce the statistics of about 20% and 50% for SD and CD, respectively.

3.4 Corrections

3.4.1 Monte Carlo Embedding Technique

The correction factors are obtained by the multistep embedding MC technique. First, simulated tracks are blended into real events at the raw data level. Real data events to be used in the embedding are sampled over the entire data-taking period in order to have proper representation of the whole data set used in the analysis. Three samples of embedding MC were produced:

1. The MC track kinematics are taken from flat distributions in η and p_T. The flat p_T distribution is used in order to have similar statistics in different p_T bins.

2. PYTHIA 8.186 SD with Schüler and Sjöstrand Pomeron Flux model ([14]).

3. PYTHIA 8.186 CD with Minimum Bias Rockefeller Pomeron Flux model ([14]).

The tracks are propagated through the full simulation of the STAR detector and geometry using GEANT with a realistic simulation of the STAR-TPC response. The obtained raw data information for the simulated particles are added on to the existing information of the real data. Next, the mixed events are treated just as real data and are processed through the full reconstruction chain.

3.4.2 Data-MC comparison

The most critical quality assurance is to make sure that the MC simulation reproduces the characteristics of the real data. This is carried out by comparing various distributions from real data and from embedding MC as shown in Figures 3.15 to 3.23. Good agreement is found between embedding MC and real data.
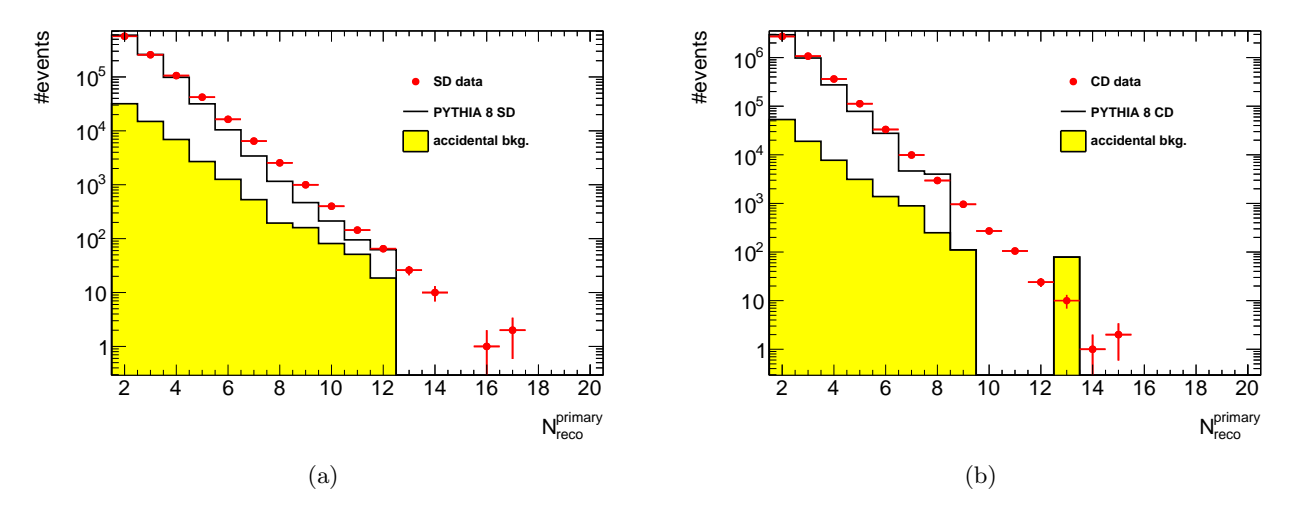
(a) (b)

Figure 3.15: Comparison of number of primary tracks distributions for SD and CD collisions between embedding MC and real data. In SD and CD $p + p$ collisions, the average number of tracks per event is small compared to non-diffractive $p + p$ collisions.
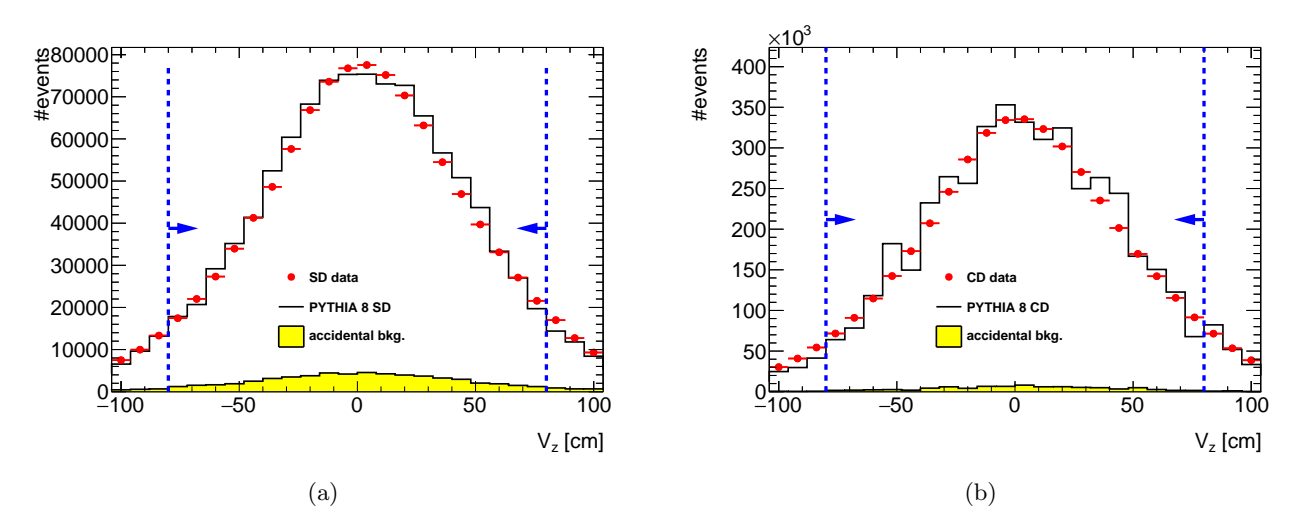

(a) (b)

Figure 3.16: Comparison of the z component of the primary vertex, V_z, distributions for SD and CD collisions between embedding MC and real data. Blue lines and arrows indicate region accepted in analysis.
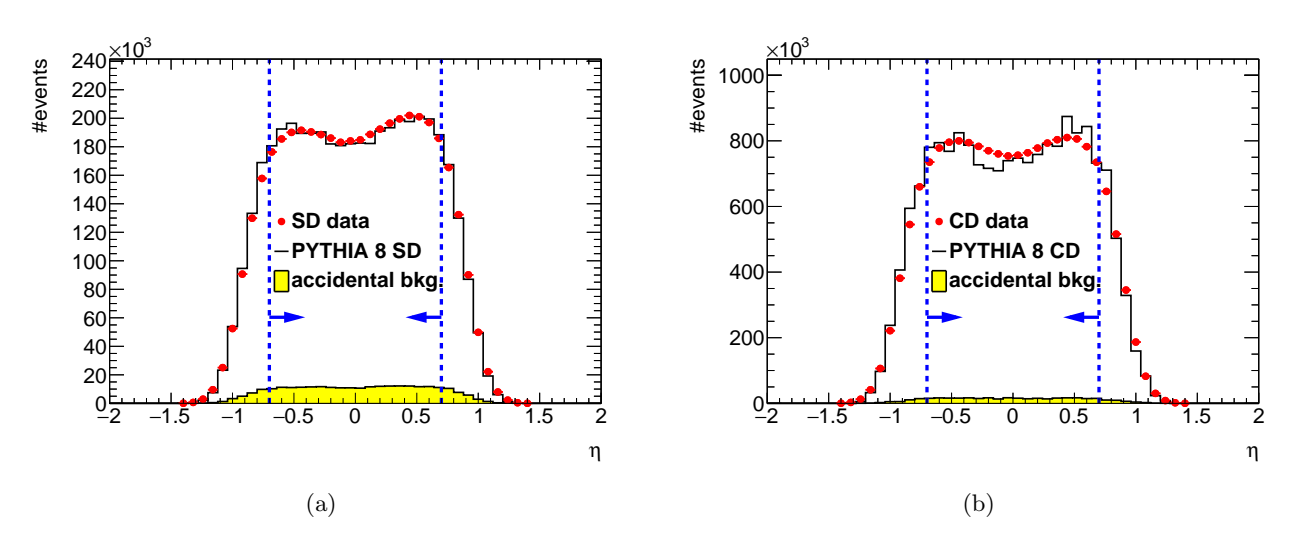

(a) (b)

Figure 3.17: Comparison of the pseudorapidity, η, distributions for SD and CD collisions between embedding MC and real data. Blue lines and arrows indicate region accepted in analysis.
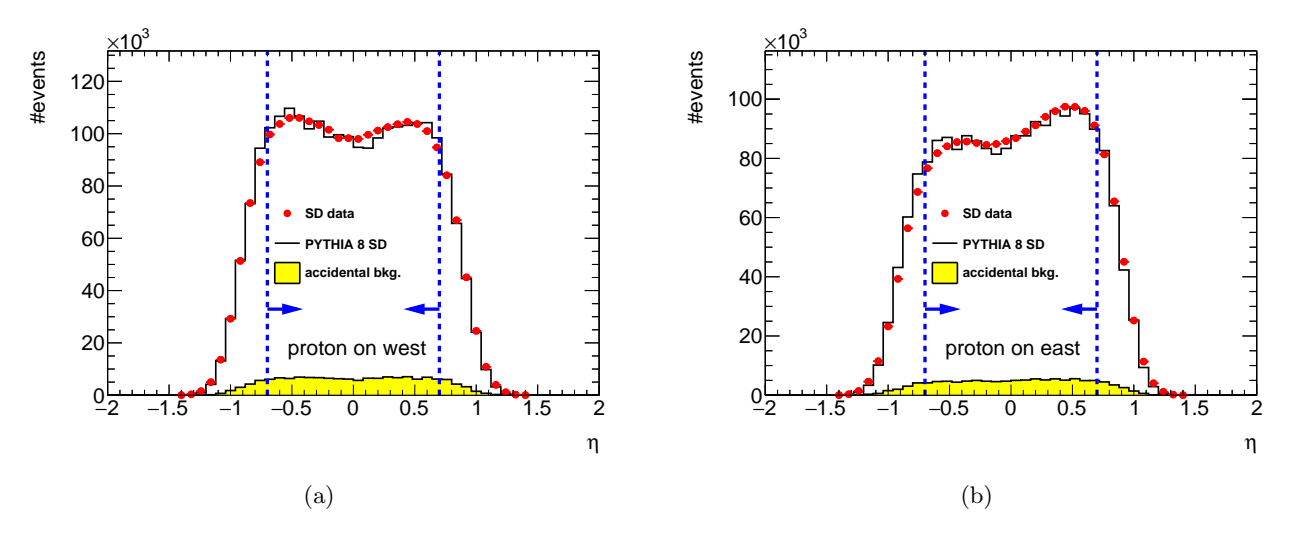
(a)   (b)

Figure 3.18: Comparison of the pseudorapidity distributions, divided due to the outgoing proton direction, for SD collisions between embedding MC and real data. Blue lines and arrows indicate region accepted in analysis.
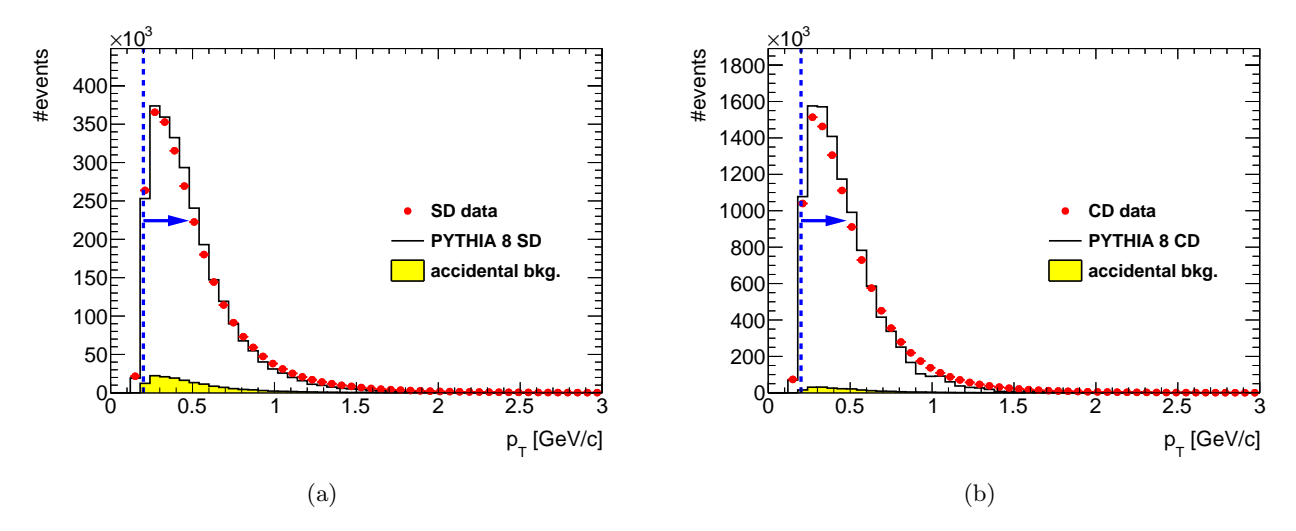

(a)   (b)

Figure 3.19: Comparison of the transverse momentum distributions, p_T, for SD and CD collisions between embedding MC and real data. Blue lines and arrows indicate region accepted in analysis.

(a)   (b)

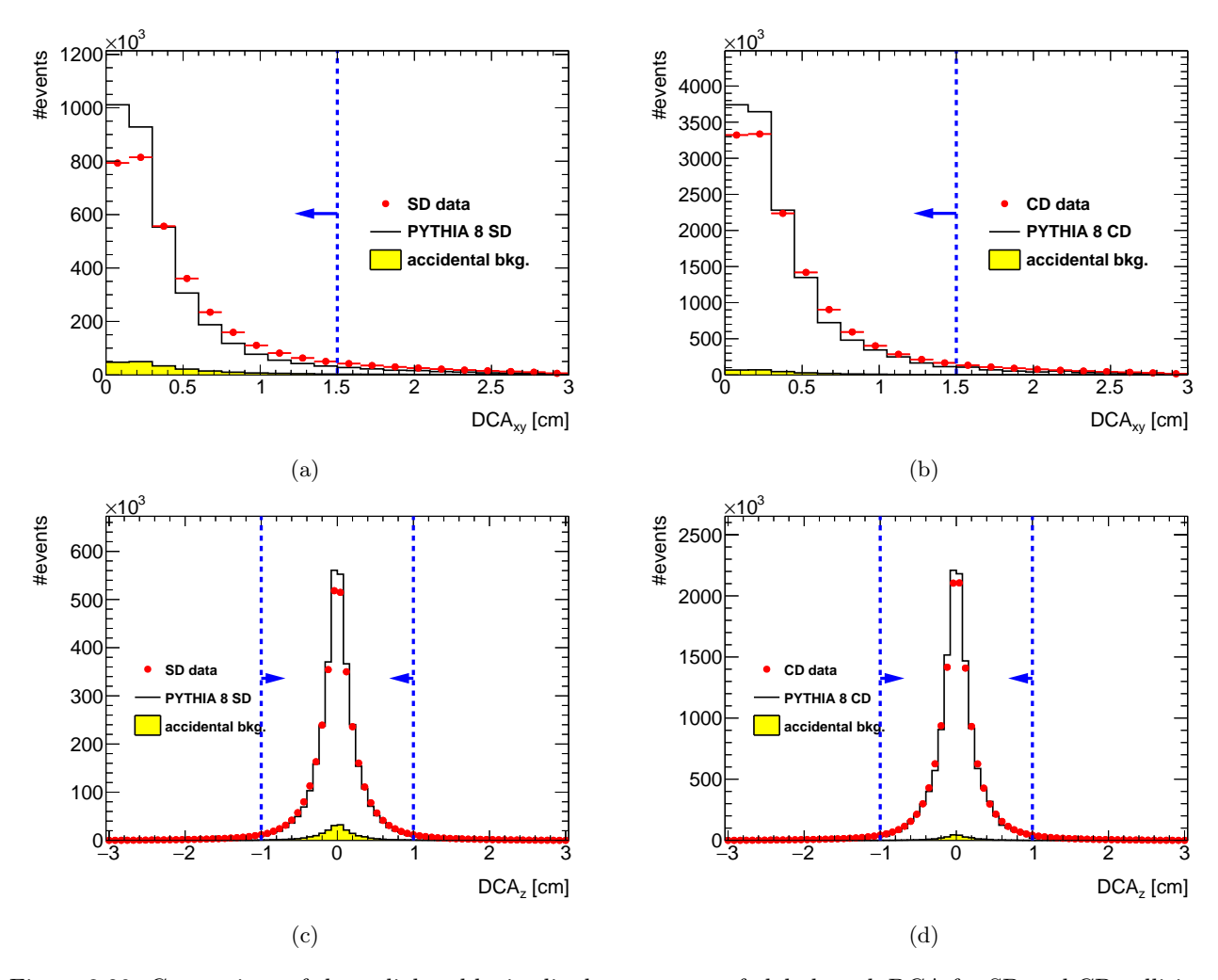(c)   (d)

Figure 3.20: Comparison of the radial and logitudinal component of global track DCA for SD and CD collisions between embedding MC and real data. Blue lines and arrows indicate region accepted in analysis.
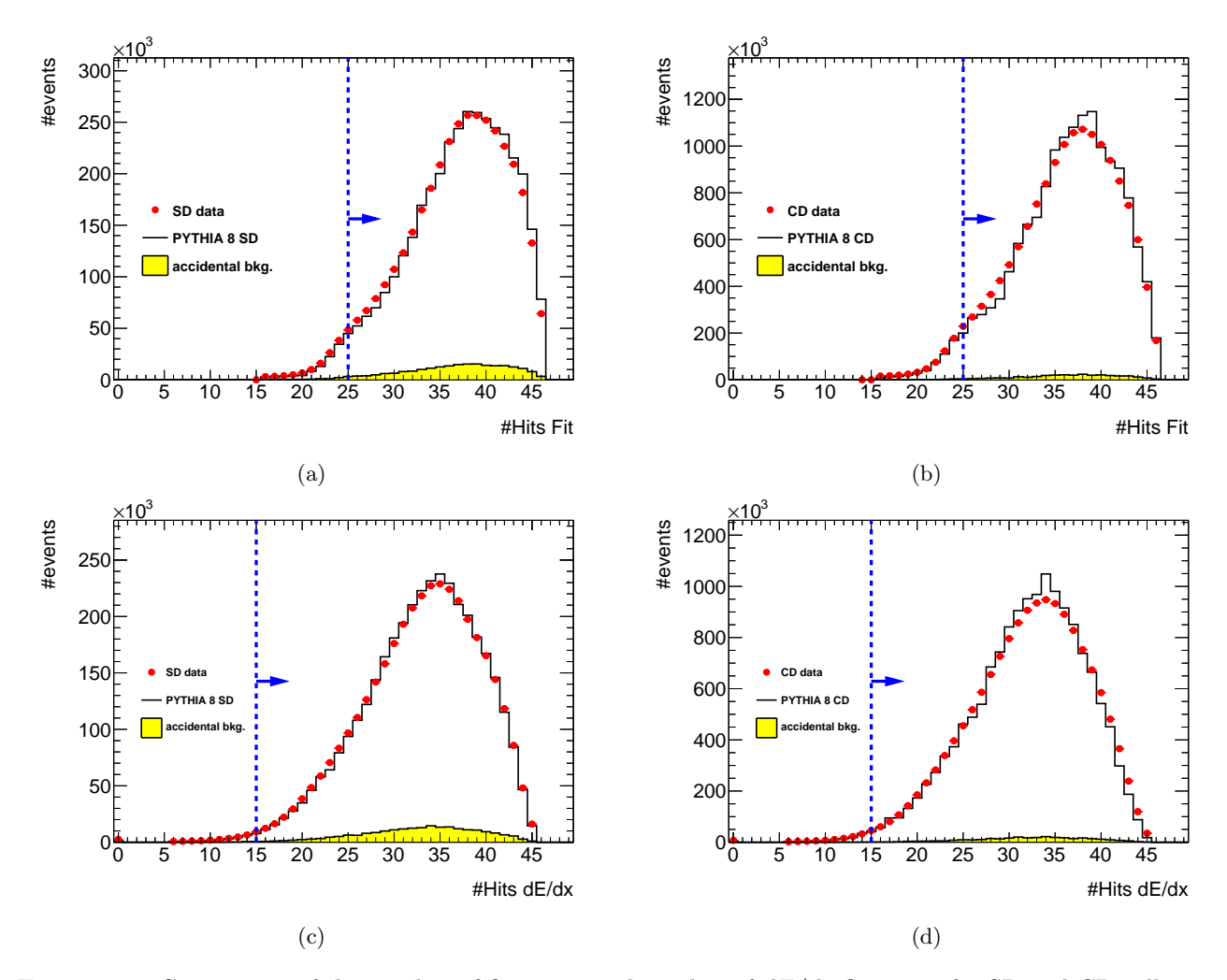
Figure 3.21: Comparison of the number of fit points and number of dE/dx fit points for SD and CD collisions between embedding MC and real data. Blue lines and arrows indicate region accepted in analysis.
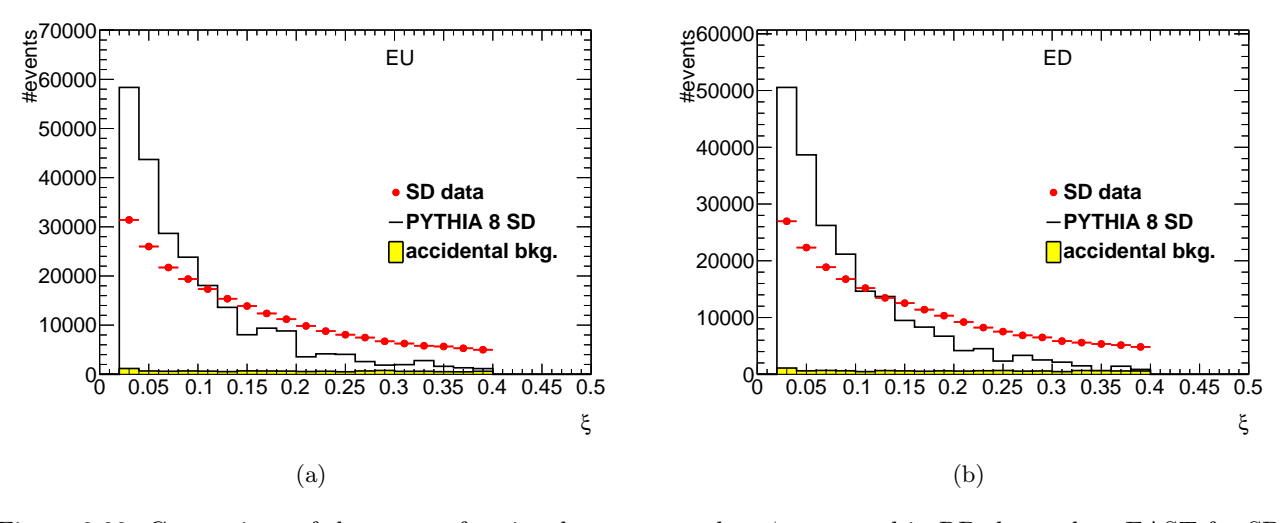

Figure 3.22: Comparison of the proton fractional momentum loss ξ measured in RPs located on EAST for SD collisions between embedding MC and real data.
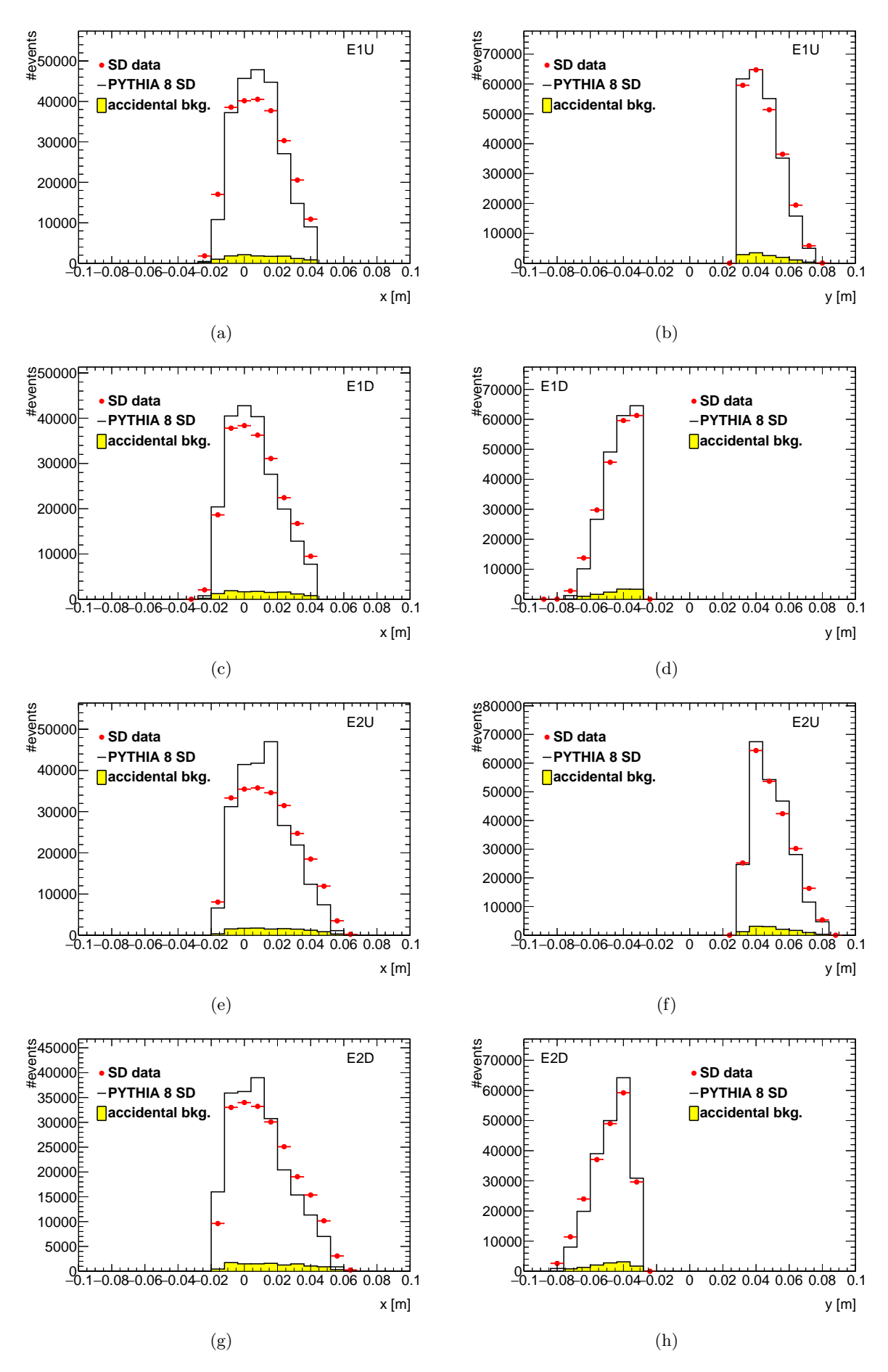
Figure 3.23: Comparison of the proton position measured in RPs located on EAST for SD collisions between embedding MC and real data.

3.4.3 Vertex reconstruction

In *pp* collisions, where the charged-particle multiplicity is low, the vertex finding algorithm sometimes fails to find a primary vertex. In addition, at high luminosity, vertex finder can fail due to the contribution of pile-up events and providing a wrong reconstructed vertex. In this study we require at least two reconstructed global tracks $N_{reco}^{global} \geq 2$ passing all the quality cuts listed in Table 3.1 but without DCA_{xy} and DCA_z cuts.

Track quality cuts used for vertexing

A global track used in vertex reconstruction has to pass the quality cuts listed in the Table 3.2, which are different than used in the analysis. Since that, vertex reconstruction efficiency and fake vertex rate is calculated as a function of number of global tracks used in vertexing N_{vrt}^{global} instead of N_{reco}^{global}.

Quantity	Cut
Number of Fit Points	Fit Points > 20
Transverse Impact Parameter	$|d_0| < 2$ cm
Ratio of Fit Points / Possible Fit Points	Fit Points/ Possible Fit Points > 0.52
Global Track Transverse Momentum	$p_T > 0.2$ GeV/c
TOF Matched Track	TOF Match-Flag ≥ 1

Table 3.2: Vertexing Track Level Cuts

Vertex efficiency and fake vertex

In every MC event there is a well defined primary vertex. With the embedded event reconstructed and the MC information in hand, the vertex-finding efficiency can be obtained. In the analysis we require exactly one reconstructed vertex with at least two primary tracks passing the selection cuts $N_{reco}^{primary} \geq 2$. The vertex with the label *best* is the one with the highest number of TOF-matched tracks. If there are more than one such vertices, the *best* vertex is the one with the higher rank in the MuDst. The following studies were done for events with the *z*-coordinate of the true-level primary vertex $|V_z < 80|$ cm. The overall vertex-finding efficiency, $\epsilon_{vrt}^{best}\left(N_{vrt}^{global}\right)$, is determined as the ratio of the number of good reconstructed events (reconstructed exactly one primary vertex with at least two primary TOF-matched tracks passing the quality cuts $N_{reco}^{primary} \geq 2$), with the reconstructed vertex matched to the true-level ptimary vertex, to the number of input MC events. The fake vertex rate, $\delta_{vrt}^{fake}\left(N_{vrt}^{global}\right)$, is obtained as the ratio of the number of fake vertex events (exactly one reconstructed vertex, $N_{reco}^{primary} \geq 2$, but the reconstructed vertex not matched to the true-level primary vertex) to the number of input MC events. The vertex-finding efficiency and fake vertex rate as a function of N_{vrt}^{global} is shown in Figures 3.24a and 3.24b. Due to very large fake vertex rate ($> 50\%$) for events with many tracks, the main analysis was limited to events with $N_{reco}^{primary} < 8$ and $N_{reco}^{primary} < 6$ for SD and CD, respectively. For events with exactly two global tracks used for vertexing, $N_{vrt}^{global} = 2$, the vertex-finding efficiency and fake vertex rate were calculated as a function of the longitudinal distance between these tracks $|\Delta z_0|$, which is shown in Figures 3.24c and 3.24d. The vertex-finding efficiency is smaller than 5% for tracks with $|\Delta z_0| > 2$ cm, hence the analysis was limited to the events with $|\Delta z_0| < 2$ cm, when $N_{vrt}^{global} = 2$. Finally, each event is corrected for vertex-finding efficiency and fake vertex rate by the factor:

$$\frac{1}{\epsilon_{vrt}^{best}\left(N_{vrt}^{global}\right) + \delta_{vrt}^{fake}\left(N_{vrt}^{global}\right)} \tag{3.1}$$

Fake vertex events

From the MC study, the particle spectra from fake vertex events are extracted and compared to those from good events (with a correctly reconstructed vertex). It is found that particles from the fake vertex events have somewhat harder p_T spectra than those in good events, presumably due to the wrongly assigned reconstructed vertex to true-level primary vertex in final track fitting and the fact that higher p_T particles are assigned larger weight in the vertex-fitting algorithm. Figure 3.25 shows the ratio of the charged hadron p_T spectrum in good vertex events to that in all events with a reconstructed vertex (i.e. sum of good and fake vertex events) for SD (a) and CD (b). The spectra are normalized per event before the ratio is taken. This ratio is parameterized, and the parameterization, $\epsilon_{fake}(p_T)$, is multiplied with all p_T spectra to correct for the p_T-dependent effect of the fake vertex events.
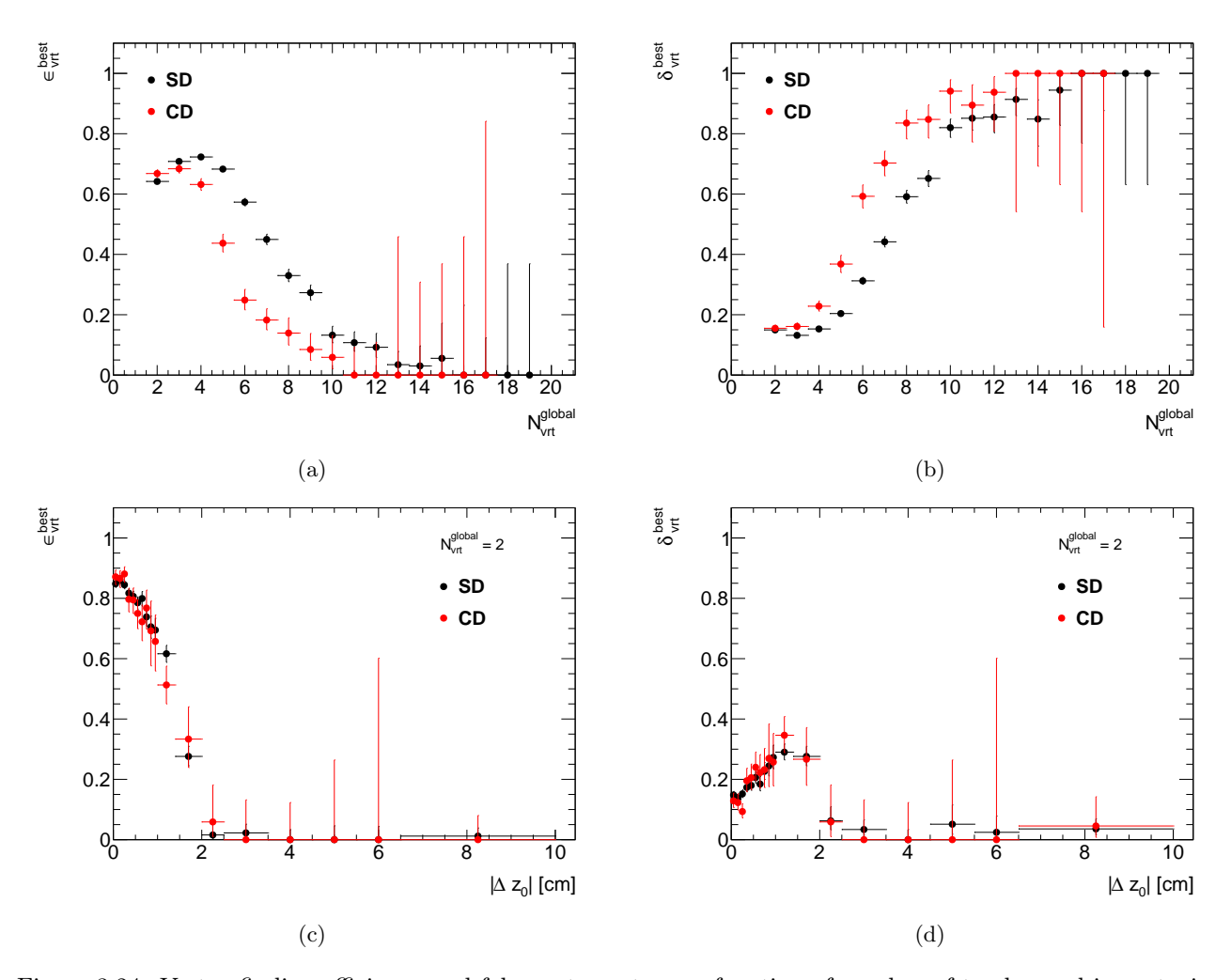
Figure 3.24: Vertex-finding efficiency and fake vertex rate as a function of number of tracks used in vertexing N_{vrt}^{global} (a-b). For events with exactly two global tracks used for vertexing, $N_{vrt}^{global} = 2$, the vertex-finding efficiency and fake vertex rate were calculated as a function of $|\Delta z_0|$ (c-d).
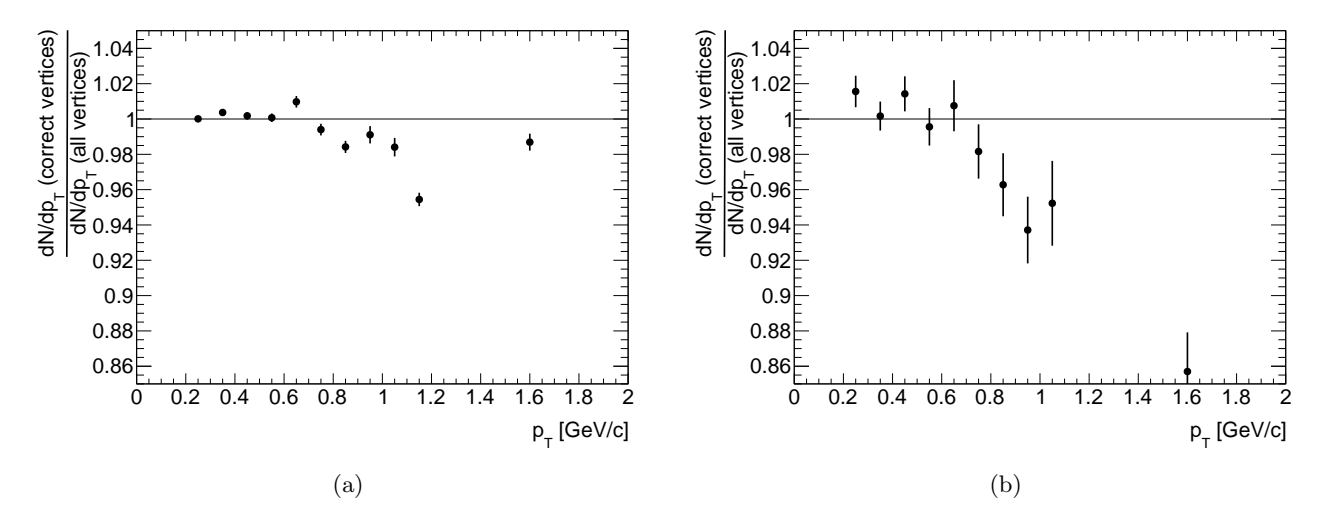

Figure 3.25: The p_T dependent correction to particle spectra due to fake vertex events, $\epsilon_{fake}(p_T)$, in SD (a) and CD (b) collisions.

Other corrections to the reconstructed vertices

As it was mentioned in the previous section, in the analysis only events with exactly one primary vertex. The data was corrected for vetoing the events due to additional vertices reconstructed as a primary vertices:

(a) more than one additional vertices

(b) secondary vertex from the interactions with the dead material

(c) fake vertex

(d) primary vertex (vertex splitting or background vertex reconstructed as best vertex)

(e) decay vertex.

The correction was obtained as a ratio of the number of events with reconstructed best vertex and additional fake/secondary vertices to all events with reconstructed best vertex as a function of N_{vrt}^{global}. As before, for events with $N_{vrt}^{global} = 2$, the correction was calculated as a function of $|\Delta z_0|$. In the end, additional term was added to the factor from the Eq. 3.1, which is used for correcting each event:

$$\frac{1}{\epsilon_{vrt}^{best}\left(N_{vrt}^{global}\right) + \delta_{vrt}^{fake}\left(N_{vrt}^{global}\right)} \cdot \frac{1}{1 - a - b - c - d - e} \qquad (3.2)$$

where $a - e$ is the fraction of events with additional vertices (labels listed above) shown in Figures 3.26 and 3.27.
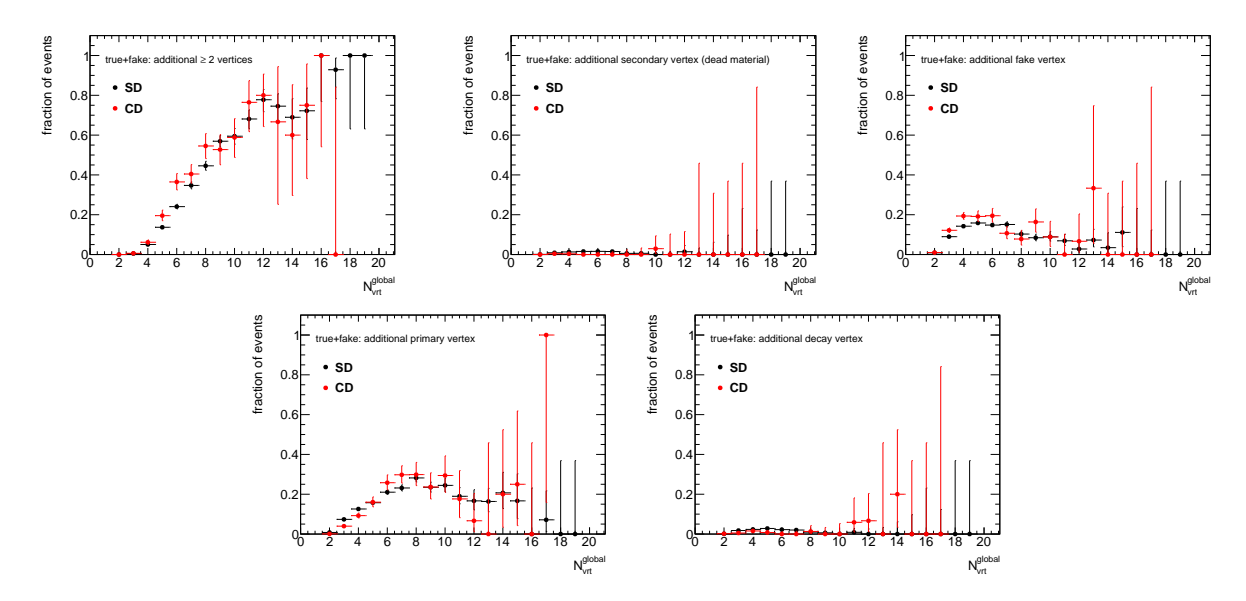
Figure 3.26: Fraction of events with reconstructed best vertex and additional reconstructed vertices as a function of N_{vrt}^{global}: more than one additional vertices (a), additional vertex from the interactions with dead material (b), additional fake vertex (c), additional primary vertex (d), additional decay vertex (e).
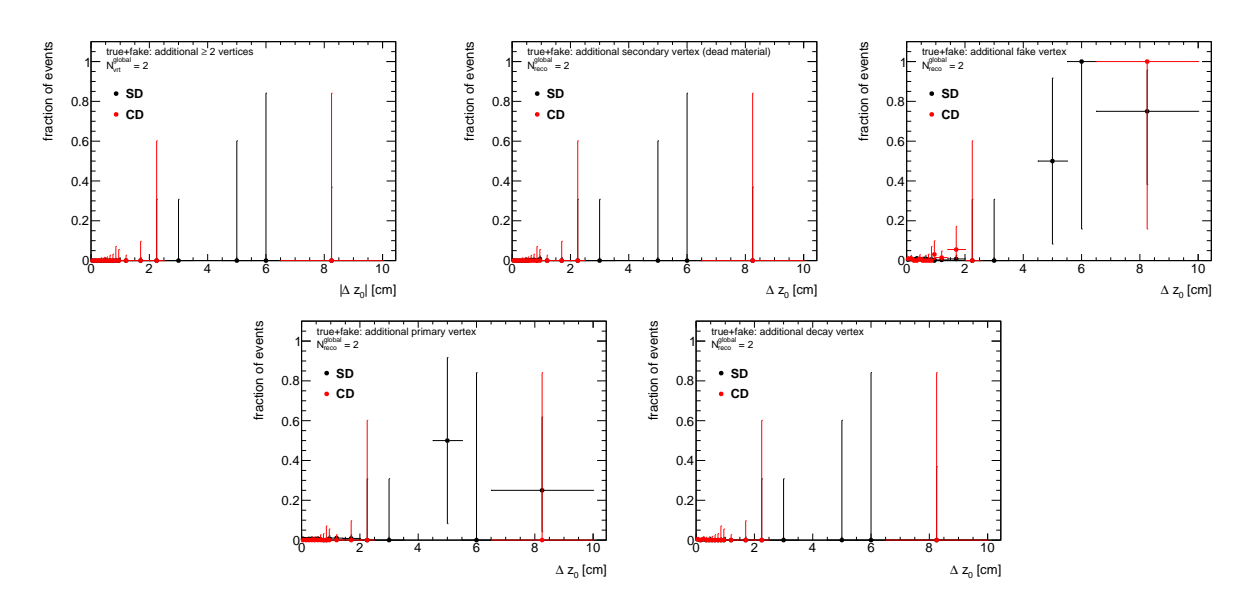
Figure 3.27: Fraction of events with reconstructed best vertex and additional reconstructed vertices as a function of $|\Delta z_0|$: more than one additional vertices (a), additional vertex from the interactions with dead material (b), additional fake vertex (c), additional primary vertex (d), additional decay vertex (e).

3.5 Inclusive charged particle distributions

3.5.1 Correction to dN/dn_{ch}

The observed $N_{reco}^{primary}$ distribution is first corrected for the vertex reconstruction efficiency. To remove the detector effects in the final results, one needs to express the multiplicity distribution in terms of the number of charged primary particles N_{ch} instead of the number of selected charged tracks $N_{reco}^{primary}$. For this, a Bayesian unfolding procedure is used [15]. Integrating the probability relation given by the Bayes theorem $P(N_{ch}) \cdot P(N_{reco}^{primary}|N_{ch}) = P(N_{ch}|N_{reco}^{primary}) \cdot P(N_{reco}^{primary})$ over $N_{reco}^{primary}$, one gets the distribution of primary particles:

$$
\begin{aligned}
N_{ev}(N_{ch}) &= \sum_{N_{reco}^{primary} \geq 0} P(N_{ch}|N_{reco}^{primary}) \cdot N_{ev}(N_{reco}^{primary}) \\
&= \frac{1}{\epsilon^{miss}(N_{ch})} \sum_{N_{reco}^{primary} \geq 2} P(N_{ch}|N_{reco}^{primary}) \cdot N_{ev}(N_{reco}^{primary})
\end{aligned}
\tag{3.3}
$$

The second relation factorizes the contribution of events that are lost due to track reconstruction inefficiency but would pass the particle level phase-space cuts, i.e. those with $N_{ch} \geq 2$ but $N_{reco}^{primary} < 2$. They are corrected for by a special factor $\epsilon^{miss}(N_{ch})$ shown in the Fig. (referencja). The unfolding procedure is done iteratively to improve the estimate of $P(N_{ch}|N_{reco}^{primary})$ taken from the MC:

- First iteration:

$$
P(N_{ch}|N_{reco}^{primary}) = P = P(N_{reco}^{primary}|N_{ch}) \frac{P^{MC}(N_{ch})}{P^{MC}(N_{reco}^{primary})}
\tag{3.4}
$$

$$
N_{ev}(N_{ch}) = \frac{1}{\epsilon^{miss}(N_{ch})} \sum_{N_{reco}^{primary} \geq 2} N_{ev}^{MC}(N_{reco}^{primary}) \cdot P
\tag{3.5}
$$

where the resolution function $P(N_{reco}^{primary}|N_{ch})$ is obtained from MC (number of tracks corresponding to a given number of particles).

- Next iterations $r + 1$:

$$
P^{r+1} = P(N_{reco}^{primary}|N_{ch}) \frac{P^r(N_{ch})}{P^r(N_{reco}^{primary})}
\tag{3.6}
$$

where normalized $N_{ev}^r(N_{ch})$ and $N_{ev}^r(N_{reco}^{primary})$ serve as probability distributions $P^r(N_{ch})$ and $P^r(N_{reco}^{primary})$.

This matrix shown in Fig. ?? is obtained using Monte Carlo and is applied to data to obtain the observed N_{ch} distribution. While the matrix is mostly populated along the diagonal, it shows events with large multiplicity at particle level, reconstructed with significantly smaller multiplicity at detector level. The total number of events, N_{ev}, is defined as the integral of the unfolded N_{ch} distribution.

3.6 Particle Identification by dE/dx

The specific ionization energy loss, the dE/dx, is a function of the particle momentum magnitude. This property is used for particle identification. This analysis focuses on particle identification in the low p_T region. This section describes the low p_T dE/dx particle identification method in detail. Extension of particle identification to high p_T is possible by the Time of Flight (TOF), $t^{TOF} = t^{stop} - t^{start}$. Due to the low particle multiplicity and lack of signal in VPDs on the outgoing proton side (rapidity gap) in SD events, the t^{start} is not defined precisely. Since that, the analysis was limited to identification only by dE/dx.

The ionization energy loss by charged particles in material is given by the Bethe-Bloch formula and for thin material by the more precise Bichsel formula[16]. With the measured particle momentum and dE/dx, the particle type can be determined by comparing the measurements against the Bethe-Bloch (Bichsel) expectation. Figure 3.28 shows the measured dE/dx versus rigidity $q \times p$ for particles in $|\eta| < 0.7$. Various bands, corresponding to different mass particles, are clearly separated at low $|q \times p|$. At modest $|q \times p|$, the bands start to overlap: $e^{\pm}$ and $K^{\pm}$ merge at ~ 0.4 GeV/c, $K^{\pm}$ and $\pi^{\pm}$ merge at ~ 0.7 GeV/c, and $p(\bar{p})$ and $\pi^{\pm}$ merge at ~ 1.1 GeV/c. However, particles can still be statistically identified by a fitting procedure. The separation of the dE/dx bands depends on the pseudorapidity region and decreases toward higher rapidities. In the midrapidity region of $|\eta| < 0.7$, p_T is approximately equal to $|p|$.
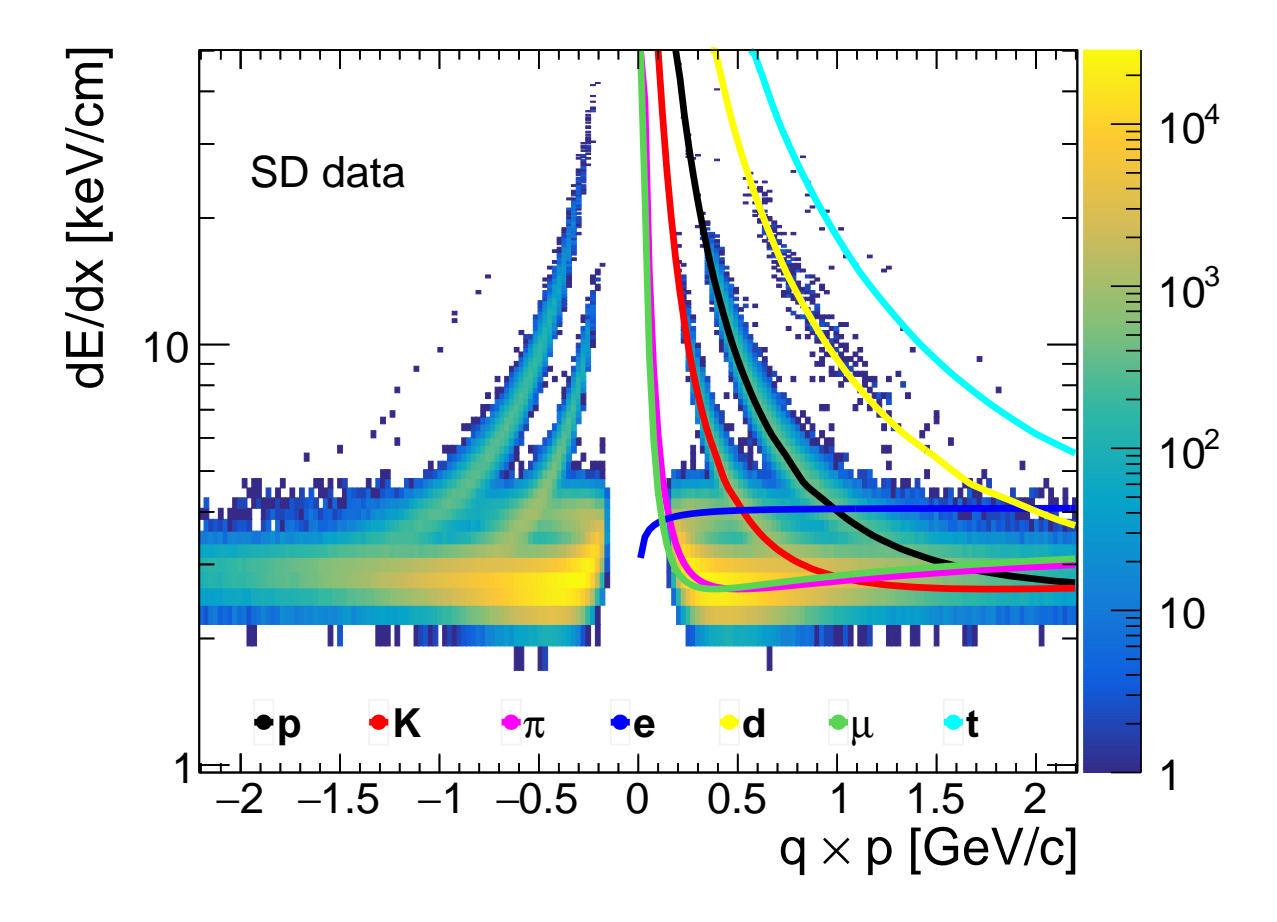
Figure 3.28: Specific ionization energy loss dE/dx as a function of rigidity $q \times p$ for particles in $|\eta| < 0.7$ measured in 200 GeV SD pp collisions by the STAR-TPC. The Bichsel predictions for each particle species are also shown.

Since the dE/dx distribution for a fixed particle type is not Gaussian, a new variable is useful in order to have a proper deconvolution into Gaussians. A better Gaussian variable, for a given particle type, is the $n\sigma^i_{dE/dx}$-variable, defined as

$$n\sigma^i_{dE/dx} = \ln\left(\frac{dE/dx}{(dE/dx)^{BB}_i}\right)/\sigma \qquad (3.7)$$

where $(dE/dx)^{BB}_i$ is the Bethe-Bloch (Bichsel) expectation of dE/dx for the given particle type $i(i = \pi, K, p)$, σ - the dE/dx resolution. The expected value of $n\sigma^i_{dE/dx}$ for the particle in study is around 0 and the width equals to 1. The $n\sigma^i_{dE/dx}$ is shown for $\pi^{\pm}$, $K^{\pm}$ and $p(\bar{p})$ in Fig. 3.29.
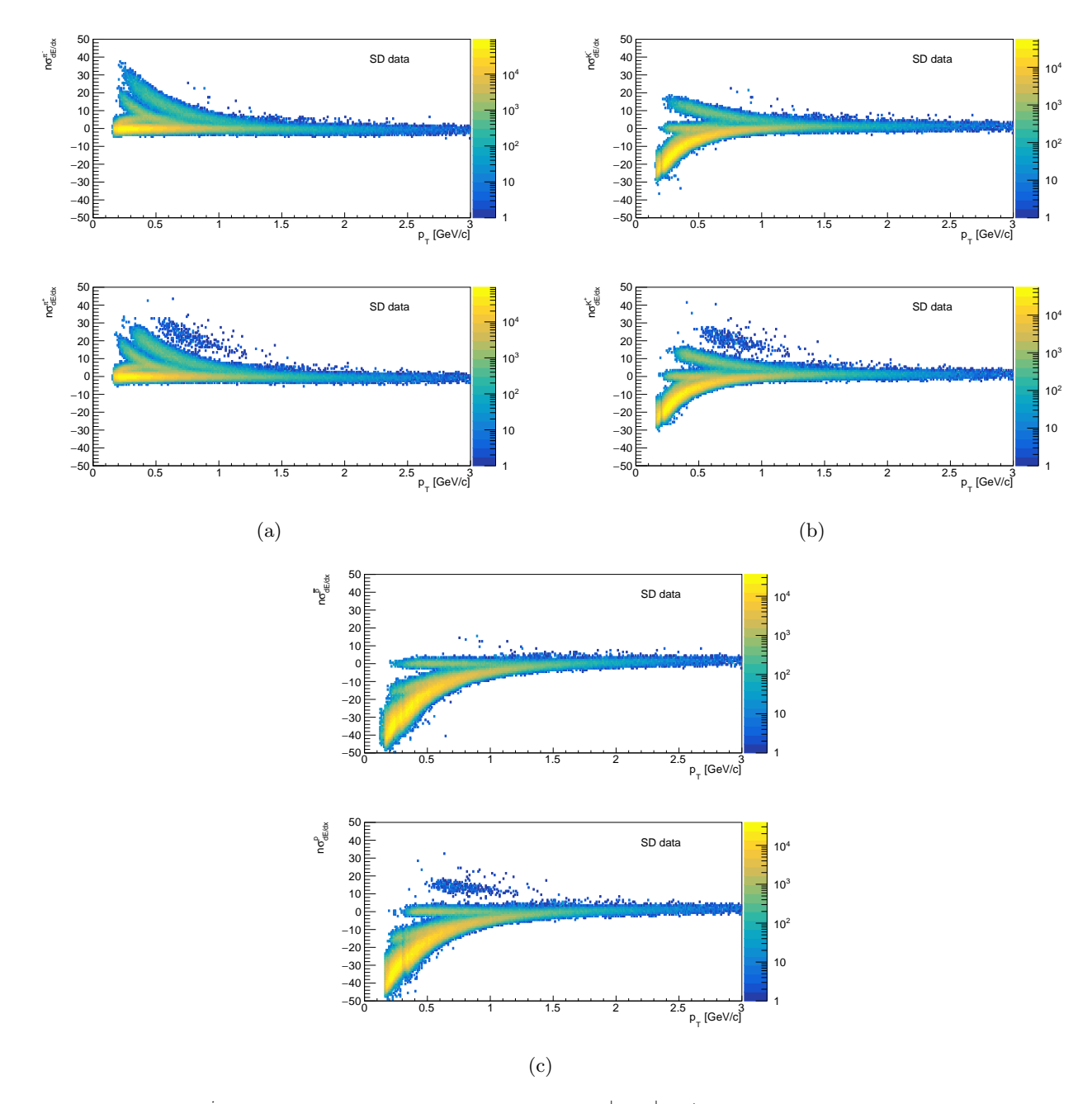
(a)

(b)

(c)

Figure 3.29: The $n\sigma^i_{dE/dx}$ variable for particle i, where $i = \pi^\pm, K^\pm, p/\bar{p}$, versus p_T in SD collisions. Particles are restricted in $|\eta| < 0.7$ and corrected for the energy loss (mass of i-particle was taken) and vertexing. In this narrow pseudorapidity slice, p_T is approximately equal to $|p|$.

Figure 3.30 shows the $n\sigma^{\pi^\pm}_{dE/dx}$, $n\sigma^{K^\pm}_{dE/dx}$ and $n\sigma^{p(\bar{p})}_{dE/dx}$ distributions for one p_T bin, each corrected for the energy loss[17] (mass of i-particle was taken) and vertexing (other p_T bins are shown in Appendix A). To extract the particle yield for a given particle type, a multi-Gaussian fit is applied to the $n\sigma^i_{dE/dx}$ distribution as shown in Fig. 3.30. The parameters of the multi-Gaussian fit are the centroids μ_{i^-/i^+}, widths σ_{i^-/i^+}, sum and ratios of amplitudes C_{i^-/i^+}, r_{i^-/i^+} for negative i^- and positive i^+ particles ($\pi^\pm$, $e^\pm$, $K^\pm$, p and $\bar{p}$). The positive and negative particle $n\sigma^i_{dE/dx}$-distributions are fit simultaneously. The particle and antiparticle centroids and widths are kept the same. Additionally, there are some assumptions depending on particle under study:

1. $\pi^\pm$ fit:

   - $p_T > 0.35$ GeV/c: r_{e^-/e^+} and C_{e^-/e^+} are fixed to the MC prediction and scaled by the ratio of the fit result in bin with $0.3 < p_T < 0.35$ GeV/c to the MC prediction in that bin.
   - $p_T > 0.4$ GeV/c: electron width σ_{e^-/e^+} is extrapolated from the lower-p_T bins and fixed.
   - $p_T > 0.55$ GeV/c: kaon width σ_{K^-/K^+} is extrapolated from the lower-p_T bins and fixed.

29

- $p_T > 0.75$ GeV/c: proton width $\sigma_{\bar{p}/p}$ is extrapolated from the lower-p_T bins and fixed.

2. $K^{\pm}$ fit:

- $p_T > 0.4$ GeV/c: r_{e^-/e^+} and C_{e^-/e^+} are fixed to the MC prediction and scaled by the ratio of the fit result in bin with $0.35 < p_T < 0.4$ GeV/c to the MC prediction in that bin.

- $p_T > 0.4$ GeV/c: electron mean μ_{e^-/e^+} is fixed to the MC prediction (dE/dx in MC is corrected[17]).

3. $\bar{p}/p$:

- $p_T > 0.55$ GeV/c: pion and kaon widths σ_{π^-/π^+} and σ_{K^-/K^+} are kept the same.

(a)

(b)

(c)
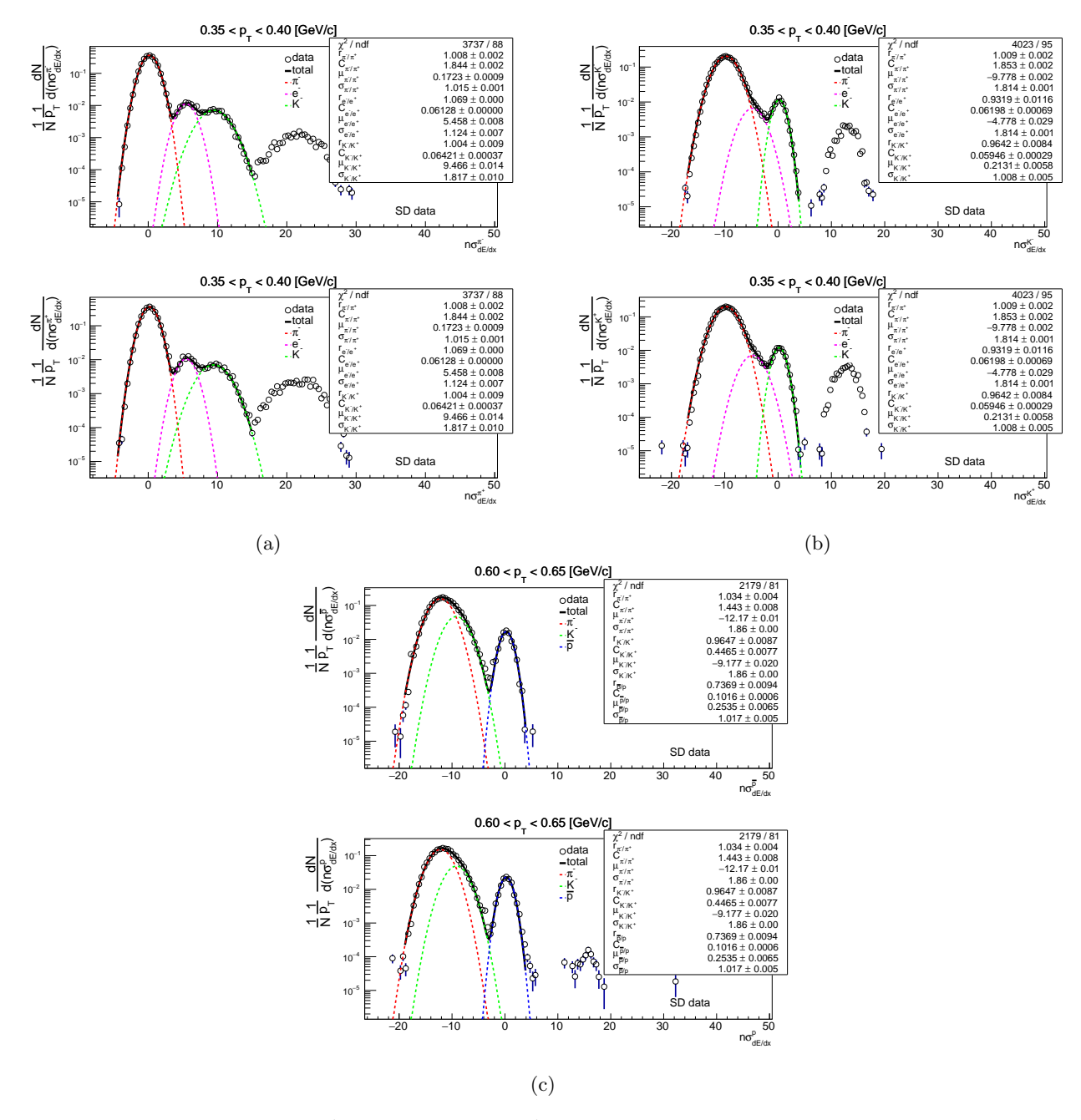
Figure 3.30: Distributions of $n\sigma_{dE/dx}^{\pi^{\pm}}$ for $\pi^{\pm}$ (a), $n\sigma_{dE/dx}^{K^{\pm}}$ for $K^{\pm}$ (b) and $n\sigma_{dE/dx}^{\bar{p}/p}$ for $\bar{p}/p$ (c) in SD collisions. One p_T bin is shown for each particle species. Particles are corrected for the energy loss and vertexing. The curves represent the Gaussian fits to the $n\sigma_{dE/dx}^{i}$ distributions, with individual particle peaks plotted separately.

The particle yield is extracted from the fit to the corresponding $n\sigma_{dE/dx}^{i}$ distribution (corrected only for the energy loss and vertexing). The fit yields for the other particle peaks can not be used, because the energy

loss correction calculation is incorrect for those particle types. Thus, the same procedure is repeated for each particle type separately. As shown in Fig. 3.29, particle identification as a function of transverse momentum is limited due to the merging of the dE/dx bands at large p_T. Pions can be identified in the momentum range of $0.2 - 0.75$ GeV/c, kaons $0.3 - 0.6$ GeV/c and (anti)protons $0.4 - 1.1$ GeV/c. Kaon identification is difficult because electrons are merged into the kaon band above $p_T > 0.4$ GeV/c.

A. Distributions of $n\sigma^i_{dE/dx}$ in SD
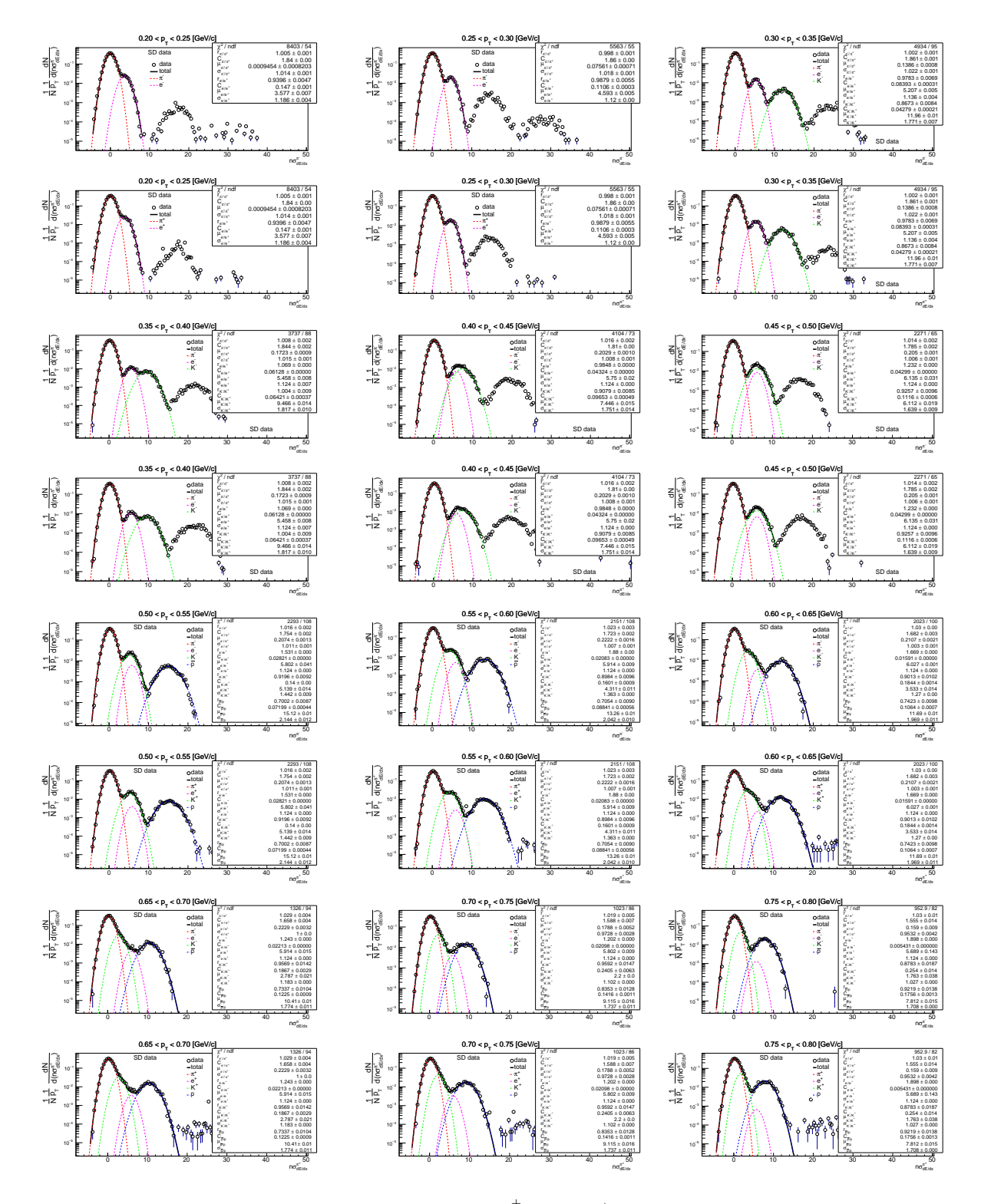
Figure A.1: Distributions of $n\sigma^{\pi^\pm}_{dE/dx}$ for $\pi^\pm$ in SD collisions.
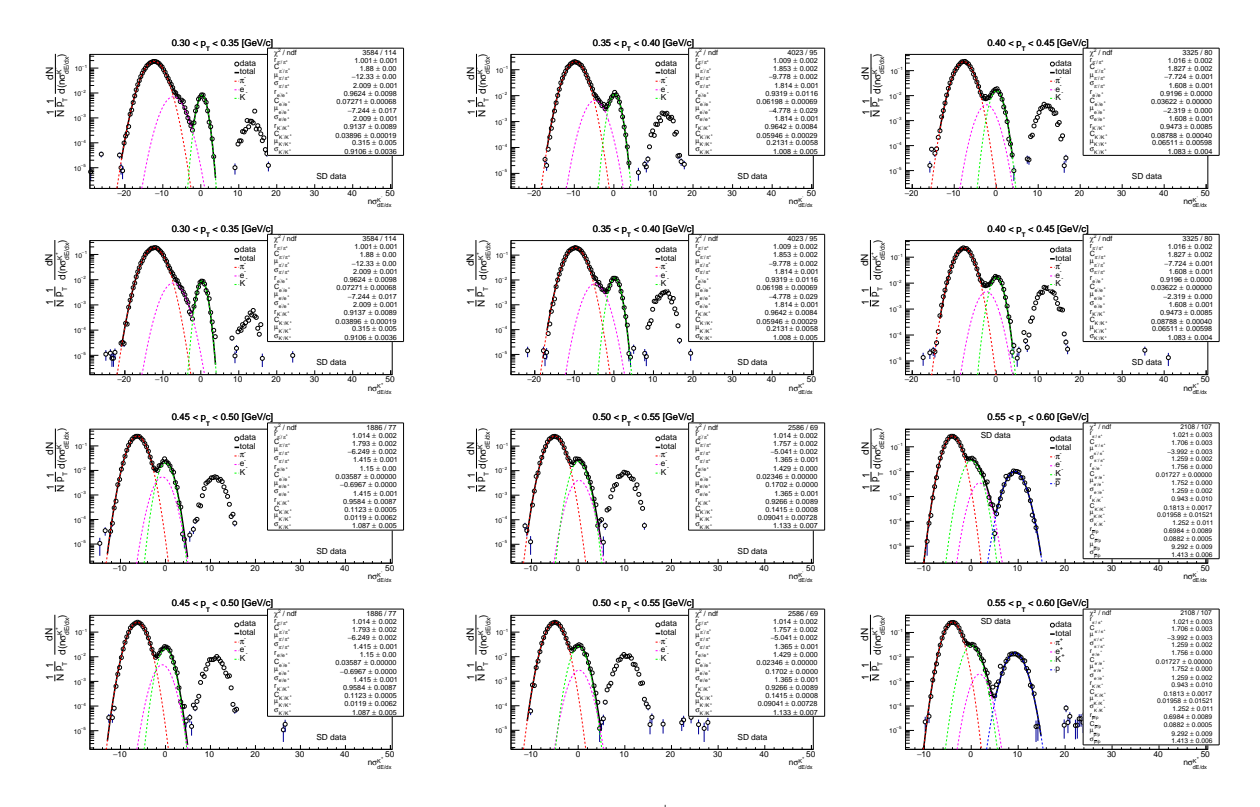
Figure A.2: Distributions of $n\sigma_{dE/dx}^{K^{\pm}}$ for $K^{\pm}$ in SD collisions.
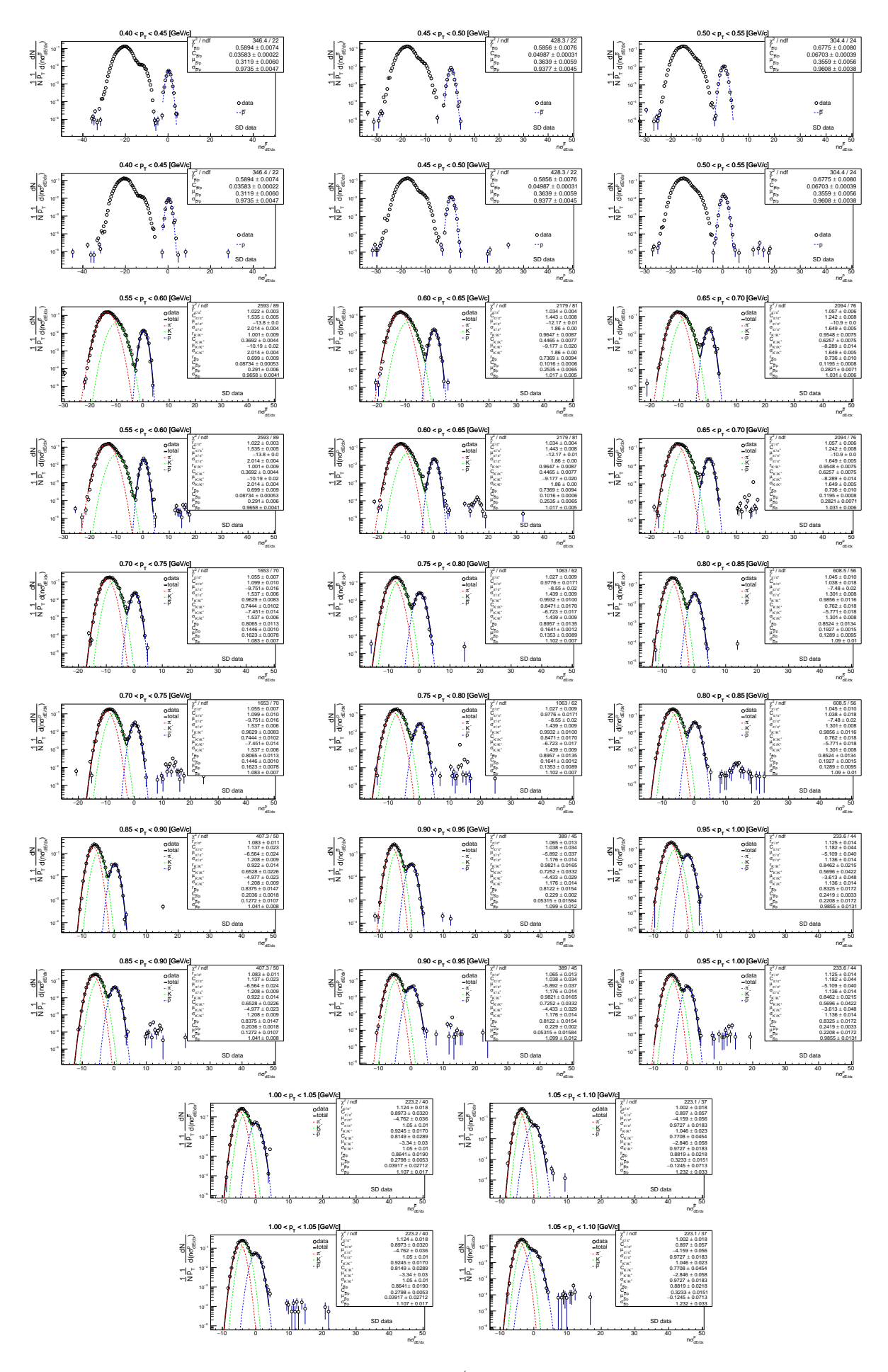
Figure A.3: Distributions of $n\sigma_{dE/dx}^{\bar{p}/p}$ for $\bar{p}/p$ in SD collisions.

List of Figures

List of Tables

References

[1] V. Barone and E. Predazzi, *High-Energy Particle Diffraction*. Springer, 2002.

[2] S. Donnachie, G. Dosch, P. Landshoff, and O. Nachtmann, *Pomeron Physics and QCD*. Cambridge Monographs on Particle Physics, Nuclear Physics and Cosmology. Cambridge University Press, 2002.

[3] B. Abelev, M. Aggarwal, Z. Ahammed, B. Anderson, D. Arkhipkin, K. Krueger, H. Spinka, and D. Underwood, "Systematic measurements of identified particle spectra in pp, d+au, and au+au collisions at the star detector.," *Physical Review C: Nuclear Physics* **79** (2009) – ,. 10.1103/PhysRevC.79.034909.

[4] **ALICE** Collaboration, J. Adam *et al.*, "Measurement of pion, kaon and proton production in proton–proton collisions at $\sqrt{s} = 7$ TeV," *Eur. Phys. J.* **C75** no. 5, (2015) 226, `arXiv:1504.00024` `[nucl-ex]`.

[5] B. Z. Kopeliovich and B. G. Zakharov, "Novel Mechanisms of Baryon Number Flow Over Large Rapidity Gap," *Z. Phys.* **C43** (1989) 241.

[6] G. C. Rossi and G. Veneziano, "A Possible Description of Baryon Dynamics in Dual and Gauge Theories," *Nucl. Phys.* **B123** (1977) 507–545.

[7] F. W. Bopp, "Central baryons in dual models and the possibility of a backward peak in diffraction," `arXiv:hep-ph/0002190 [hep-ph]`.

[8] **ALICE** Collaboration, K. Aamodt *et al.*, "Midrapidity antiproton-to-proton ratio in pp collisions at $\sqrt{s} = 0.9$ and 7 TeV measured by the ALICE experiment," *Phys. Rev. Lett.* **105** (2010) 072002, `arXiv:1006.5432 [hep-ex]`.

[9] B. Kopeliovich and B. Povh, "Baryon stopping at HERA: Evidence for gluonic mechanism," *Phys. Lett.* **B446** (1999) 321–325, `arXiv:hep-ph/9810530 [hep-ph]`.

[10] `https://online.star.bnl.gov/rp/pp200/`.

[11] `https://online.star.bnl.gov/RunLogRun15/`.

[12] `https://drupal.star.bnl.gov/STAR/event/2017/09/27/software-and-computing-meeting/revertexing-2015-rp-stream`.

[13] `https://drupal.star.bnl.gov/STAR/system/files/talk_42.pdf`.

[14] "PYTHIA 8 manual." `http://home.thep.lu.se/~torbjorn/pythia81html/Welcome.html`.

[15] G. D'Agostini, "A multidimensional unfolding method based on bayes' theorem," *Nuclear Instruments and Methods in Physics Research Section A: Accelerators, Spectrometers, Detectors and Associated Equipment* **362** no. 2, (1995) 487 – 498. `http://www.sciencedirect.com/science/article/pii/016890029500274X`.

[16] H. Bichsel, "A method to improve tracking and particle identification in TPCs and silicon detectors," *Nucl. Instrum. Meth.* **A562** (2006) 154–197.

[17] L. Adamczyk, L. Fulek, and R. Sikora, "Supplementary note on diffractive analyses of 2015 proton-proton data." `https://github.com/rafalsikora/DiffractiveAnalyses_CommonNote/blob/master/DiffractiveAnalyses_AnalysisNote.pdf`.